Supporting Information

Interfacial and Electronic Modulation of FeP-CoP on Reduced Graphene Aerogel Boosts Bifunctional Catalysis for Overall Water Splitting

Yifeng Xue [a], Mingyue Qiu [a], Jie Luo [a], Hongke Qiao [b], Tianyi Yang [a], Hong Chen [a], Guiyu Zhu [a], Xiaoli Li [c], Lu Zou [a], Xiaoxiao Zhang [a], Jianzhi Wang [a,*], Faquan Yu [a,*]

[a] *Key Laboratory for Green Chemical Process of Ministry of Education, Hubei Key Laboratory for Novel Reactor and Green Chemistry Technology, State Key Laboratory of Green and Efficient Development of Phosphorus Resources, School of Chemical Engineering and Pharmacy, Wuhan Institute of Technology, Wuhan 430205, Hubei, China*

[b] *School of Chemistry and Chemical Engineering, Ningxia University, Ningxia 75300, China*

[c] *College of Earth and Environmental Sciences, Lanzhou University, Lanzhou, 730000, China*

*Corresponding authors. *E-mail addresses*: wangjz15@163.com, fyu@wit.edu.cn

Additional Experimental Details

Samples preparation

Materials. All chemicals involved in the experiments were of analytical grade without further purification. $Co(NO_3)_2 \cdot 6H_2O$, $Fe(NO_3)_3 \cdot 9H_2O$, CH_4N_2O, NH_4F, C_2H_5OH, KOH were bought from Sinopharm Chemical Reagent Co., Ltd, $K_3Fe(CN)_6$ was bought from Macklin, Graphite oxide (GO) was purchased from Sixth Element (Changzhou) Materials Technology Co., Ltd. The material had a water content of ≤ 6 wt%, and its complete specifications are provided in **Table S16**. Hydrochloric acid (HCl) and $NaH_2PO_2 \cdot H_2O$ were bought from Shanghai Aladdin Biochemical Technology Co., Ltd. The NF (99.8%) from Cyber Electrochemical Materials Network; The water used in all experiments was filtered through an ion-exchange membrane.

Synthesis of rGA/NF. First, Graphene oxide powder was reduced by tube furnace at 200 °C for 7h, then, the NF (1 cm × 2.5 cm) was successively treated by 3 M HCl solution, ethanol and water for 10 min to remove surface impurities. Next, the freshly cleaned NF was then reacted in 50 mL of a 1.5 mg/mL rGO solution at 120 °C for 8 h under slow rotation in a homogeneous reactor. The resulting rGA/NF was taken out and washed with water thoroughly before being vacuum-dried.

Synthesis of CoCH@rGA/NF Precursor on rGA/NF. 4.5 mmol $Co(NO_3)_2 \cdot 6H_2O$, 14.25 mmol CH_4N_2O, 11.4 mmol NH_4F were dissolved in 50 ml DI water to form a clear solution. Then the clear solution and the piece of rGA/NF were poured into a Teflon-lined autoclave and then heated at 120 °C for 10 h. After dropping to room temperature, the precursor was rinsed with DI water for several times, and then placed in a vacuum drying oven at 60 °C to dry for 24 h.

Synthesis of Co-Fe PBA@rGA/NF Precursor. 0.15 g $K_3Fe(CN)_6$ was dissolved in 20 ml DI water under stirring. And CoCH@rGA/NF was put into the solution and heated at 80 °C for 24 h. After dropping to room temperature, the precursor was rinsed with DI water for several times, and then placed in a vacuum drying oven at 60 °C to dry for 24 h.

Synthesis of CoP-FeP@rGA/NF. 1.0 g $NaH_2PO_2 \cdot H_2O$ was used as the P source and it was placed at the upstream side of a tube furnace with the Co-Fe PBA@rGA/NF precursor which was put at the center. Next, Co-Fe PBA@rGA/NF precursor was annealed at 350 ℃ under argon atmosphere for 2 h in tube furnace, with a heating rate of 2 °C min^{-1}.

Synthesis of CoP-FeP/NF. The synthesis process is the same as for CoP-FeP@rGA/NF except that rGA is not used.

Synthesis of CoP@rGA/NF. The synthesis process is the same as for CoP-FeP@rGA/NF except that K3Fe(CN)6 is not used.

Synthesis of FeP@rGA/NF. The synthesis process is the same as for CoP-FeP@rGA/NF, but with $Co(NO_3)_2 \cdot 6H_2O$ replaced by $Fe(NO_3)_3 \cdot 9H_2O$ as the metal precursor.

Characterization

X-ray diffraction (XRD) patterns were recorded on RigakuD/Max2550 in the range of 5-90 using Cu-Kα radiation. Due to the overwhelming interference from the Ni foam (NF) substrate, we adopted a modified sample preparation method to accurately characterize the crystal structure of the synthesized catalysts while retaining the NF substrate as an internal reference. Specifically, most of the catalyst powder was carefully scraped off the NF substrate, but a small portion of NF was deliberately retained during

the XRD measurement. The microscopic structures of materials were intuitively observed by Field emission scanning electron microscopy (FESEM) on a ZEISS Gemini 300 microscope at 3 kV. The microstructure of the materials was observed by high-resolution transmission electron microscopy (HRTEM) on JEOL JEM-2100F. The surface composition of the sample was determined by X-ray photoelectron spectroscopy (XPS) on AXIS-ULTRA DLD using Al-Kα radiation, and the C 1s peak of contaminant carbon at 284.8 eV was adopted for calibrating the binding energies. The attenuated total reflectance surface-enhanced infrared absorption spectroscopy (ATR-SEIRAS) experiments were taken with a Thermo Nicolet 8700 spectrometer equipped with a MCT detector cooled by liquid nitrogen.

Electrochemical tests

All electrochemical measurements were performed on a Shanghai Chenhua CHI760e electrochemical workstation in a three-electrode configuration, in which the prepared catalyst was used as the working electrode, the mercury oxide electrode was used as the reference electrode, and the graphite rod was used as the counter electrode. All prepared catalysts were tested in 1 M potassium hydroxide (KOH) solution at room temperature (25 ℃), activated using cyclic voltammetry (CV) at 50 mV s^{-1} to obtain stable CV curves, HER activities were evaluated using linear sweep voltammetry at 10 mV s^{-1} and OER activities were evaluated using linear sweep voltammetry at 10 mV s^{-1}. Electrochemical impedance spectroscopy (EIS) measurements at overpotentials of 50 mV and 350 mV for HER and OER.

Electrochemical active surface area (ECSA) calculations

Electrochemical active surface areas (ECSAs) was calculated from the double layer capacitance (C_{dl}) charging curves, which was obtained from the CV curves measured in a potential scope without redox process. All potentials are corrected by 85% iR. In

the HER test, the double-layer capacitances (C_{dl}) of synthesized samples were derived from their cyclic voltammetry (CV) plots at the scan rates of 20 to 100 mV s^{-1} in the range of 0.124-0.224 V vs RHE in 1M KOH solution, and in the OER test, they were derived from their cyclic voltammetry (CV) plots at the scan rates of 20 to 100 mV s^{-1} in the range of 0.924-1.024 V. The electrochemical surface area (ECSA) is proportional to C_{dl}, based on the equation:

$$ECSA = C_{dl}/C_s$$

The specific capacitance (C_s) was chosen as 0.6 mF cm^{-2} in 1 M KOH, based on typical values reported for carbon-based materials (e.g., graphene, carbon nanotubes), owing to their high electric double-layer capacitance. .

Turnover Frequency (TOF) calculations

The loading masses of FeP-CoP@rGA and FeP-CoP catalysts on the NF substrate (with dimensions of 1 cm × 2.5 cm, yielding a total geometric area of 5 cm^2 by accounting for both sides) are 109 mg and 115.2 mg (**Table s1** and **Table s2**), corresponding to loadings of 21.8 mg cm^{-2} and 23.04 mg cm^{-2}, respectively.

Approximately 10 mg of the catalyst sample was accurately weighed and dissolved completely in 4 mL of concentrated nitric acid to obtain a clear solution. The digested solution was then transferred and diluted to the mark in a 1 L volumetric flask, followed by thorough mixing. The concentrations of Fe and Co in this solution were determined using an Model Agilent 5800 Inductively coupled plasma optical emission spectroscopy (ICP-OES).

Using the equation below, the catalysts' TOFs were determined; [1]

$$\mathrm{TOF} = \frac{JA}{4FN_s}$$

Where J is the current density at the potential, A is the surface area of the catalyst, n is the number of transferred electrons, F is the Faraday constant (96485 C mol-1)，and Ns is the molar weight of active site in the catalyst. It should be noted that the TOF values reported in this work are estimated based on the total number of metal atoms, representing a conservative lower limit. This is because the bulk atoms and potentially some surface atoms of the catalyst may not be electrochemically active.

Computation detail

DFT computational methods. All density functional theory (DFT) calculations were performed using the Vienna Ab initio Simulation Package (VASP). The projector augmented wave (PAW) method and the Perdew-Burke-Ernzerhof (PBE) exchange-correlation functional within the generalized gradient approximation (GGA) were employed. A plane-wave energy cutoff of 400 eV was used. For geometric structure optimization, due to the large size of the simulation cell, only the K-point was used for sampling the Brillouin zone. The structures were relaxed until the forces on all atoms were less than 0.01 eV/Å.

Electronic Structure Calculation

The electronic density of states (DOS) was computed through static self-consistent field (SCF) calculations based on the optimized geometry. These calculations were performed using spin-polarized density functional theory (DFT) as implemented in the VASP code. The tetrahedron method with Blöchl corrections (ISMEAR = -5) was employed for accurate DOS integration over the Brillouin zone. The projection of the DOS onto specific atoms or orbitals was analyzed using the LORBIT = 11 option.

Owing to the large size of the computational model, a 1×1×1 k-point mesh was used for structural optimization to ensure computational efficiency. For the subsequent self-consistent electronic structure calculations (e.g., for computing the density of states), a denser 3×3×1 k-point mesh was employed to achieve sufficient accuracy in Brillouin zone sampling. We constructed cells of FeP (011) and CoP (011) surfaces by cutting CoP unit cells. The optimized cell parameters are obtained as 14.76×9.84×27.74 Å, a = b = c = 90° for FeP-CoP (011), 14.76×9.84×27.74 Å, a = b = c = 90° for FeP-CoP@rGA(011) heterojunction (Figure S20). A vacuum slab of more than 15 Å was

inserted in the z direction for all models to avoid the influence of the interaction between adjacent periodic units. The K-point samplings of the Brillouin zone for different models were listed in Table S3.

OER reaction mechanism. The OER Gibbs energies were calculated by applying DFT in combination with the computational standard hydrogen electrode (SHE) model. (U = 0 V, pH = 0, p =1 bar, and T = 298.15K). Based on adsorbate evolution mechanism (AEM), followed concerted reaction path was considered.

$$* + H_2O \rightleftarrows * \mathrm{OH} + H^+ + e^- \quad (1)$$

$$* OH \rightleftarrows * \mathrm{O} + H^+ + e^- \quad (2)$$

$$* O + H_2O \rightleftarrows * \mathrm{OOH} + H^+ + e^- \quad (3)$$

$$* OOH \rightleftarrows * + O_2(\mathrm{g}) + H^+ + e^- \quad (4)$$

Where the chemical potential of the H^+/e^- is considered to estimate half of the gaseous H_2 and the H_2O molecule is considered at liquid atmospheric pressure (0.035 bar and T=298.15 K).

$$\mu_{H^+} + \mu_{e^-} = {}^1\!/_2\, \mu_{H_2(g)} \quad (5)$$

$$\mu_{H_2(g)} = E_{DFT}^{H_2(g)} + ZPE_{H_2(g)} - TS_{H_2(g)}^0 \quad (6)$$

$$\mu_{H_2O(l)} = E_{DFT}^{H_2O(l)} + ZPE_{H_2O(l)} - TS_{H_2o(l)}^0 \quad (7)$$

Where ZPE and S represent the zero-point energy correction and entropy, respectively, which are obtained from the analysis of the vibration frequency of the molecules.

HER reaction mechanism. The HER pathway was calculated in detail according to the electrochemical framework developed by Nørskov and his co-workers.

The Gibbs free energies of H adsorption were calculated as follow:

$$\Delta GH^* = \Delta EH^* + \Delta ZPE - T\Delta S = E(H^*) - E(^*) - E(H_2)/2 + \Delta ZPE - T\Delta S$$

Supporting Figures and Tables

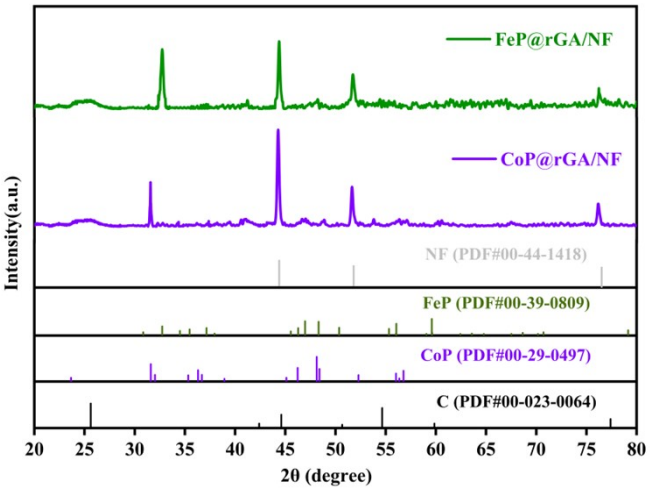

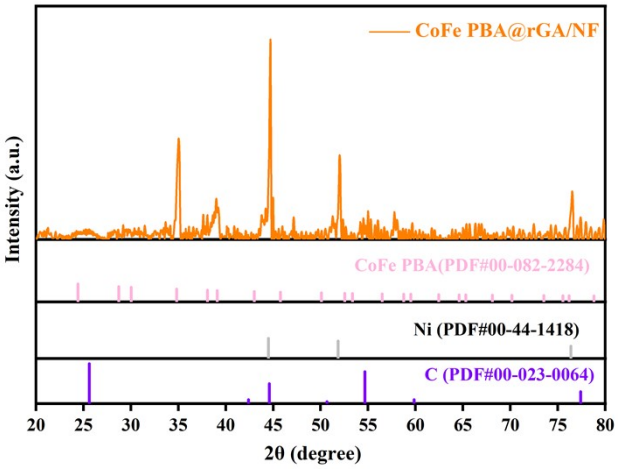

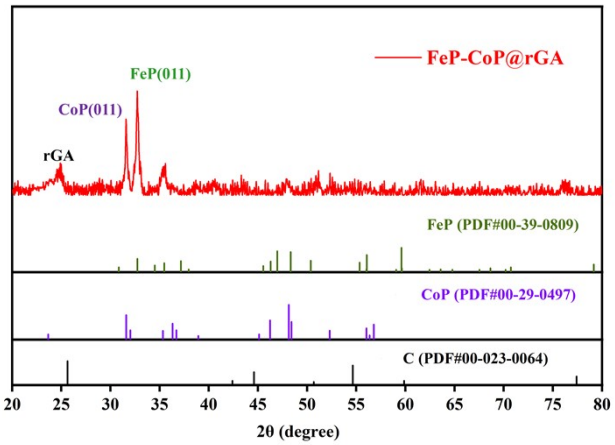

Fig. S1. XRD of FeP@rGA/NF, CoP@rGA/NF, Co-Fe PBA@rGA/NF and FeP-CoP@rGA

182

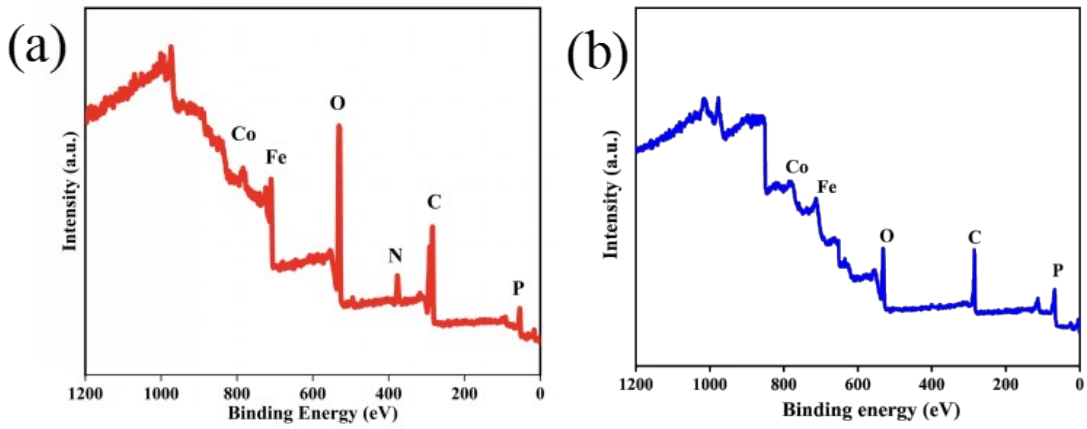

183

184 **Fig. S2**. XPS survey pattern of (a) FeP-CoP@rGA/NF and (b) FeP-CoP/NF.

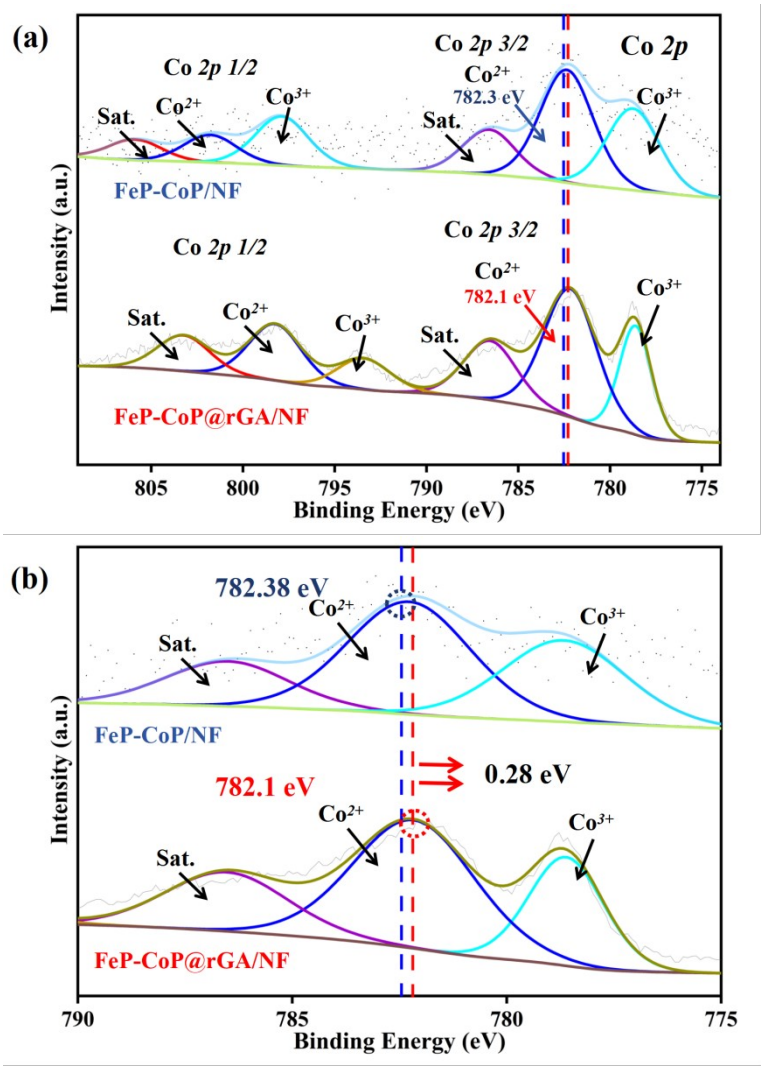

185

186

187 **Fig. S3**. The High-resolution XPS spectra difference of Co *2p* between FeP-

188 CoP/NF and FeP-CoP@rGA/NF

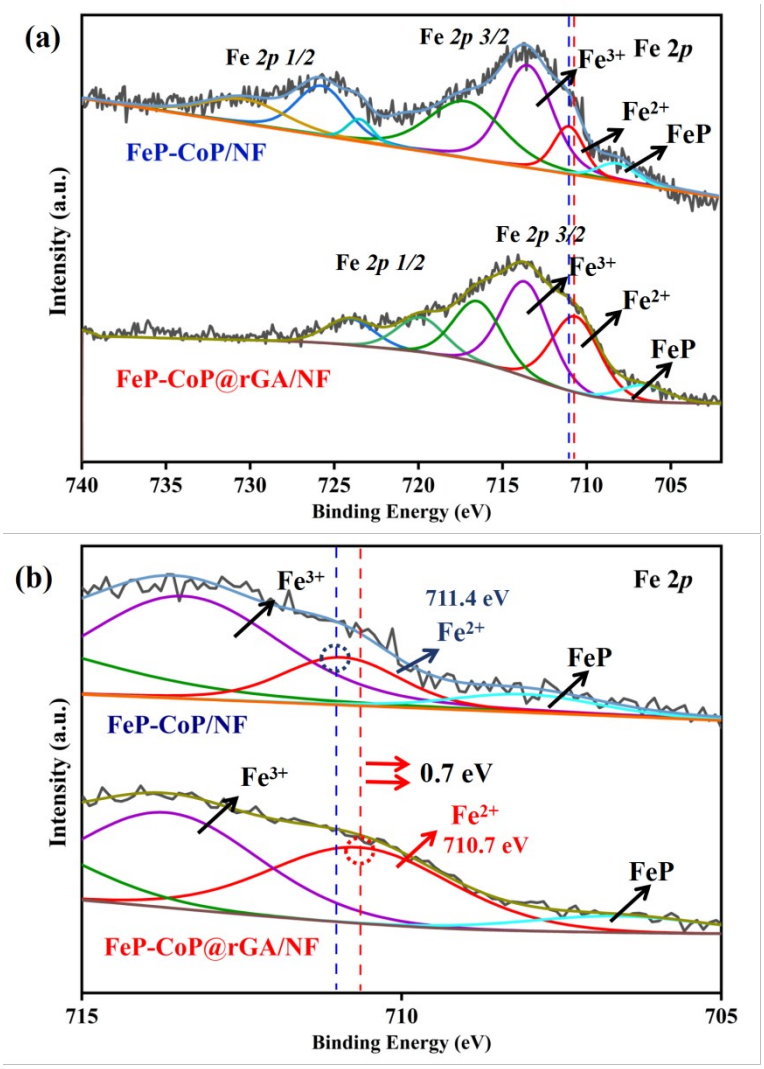

Fig. S4. The High-resolution XPS spectra difference of Fe *2p* between FeP-CoP/NF and FeP-CoP@rGA/NF

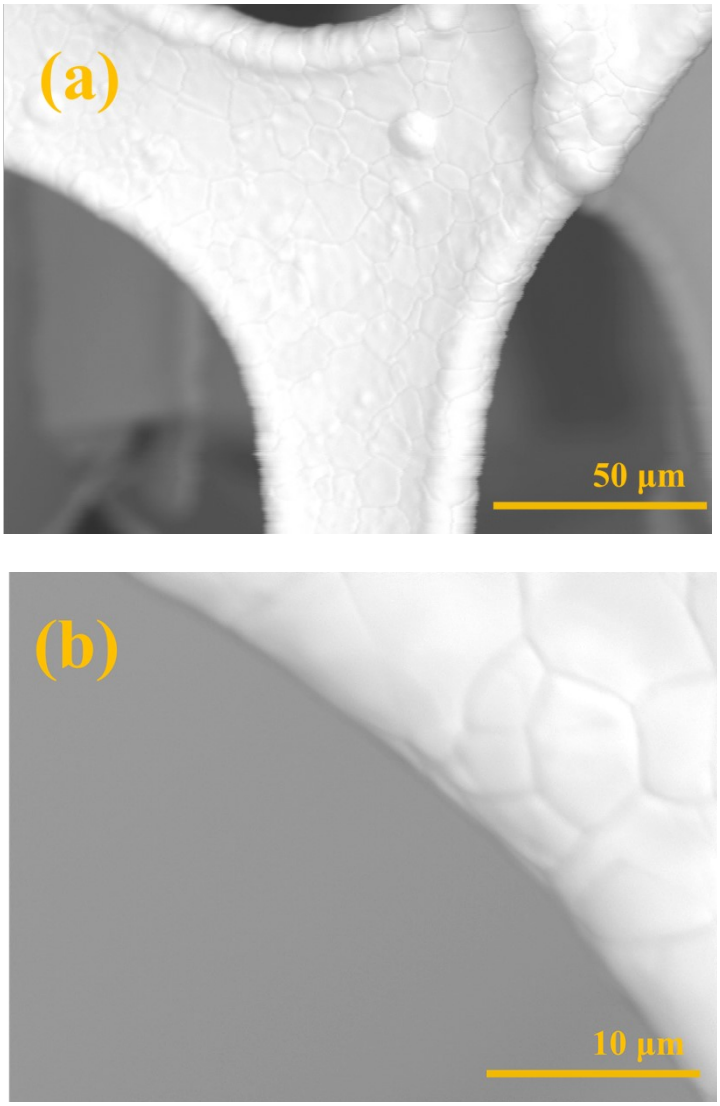

Fig. S5. SEM images of NF.

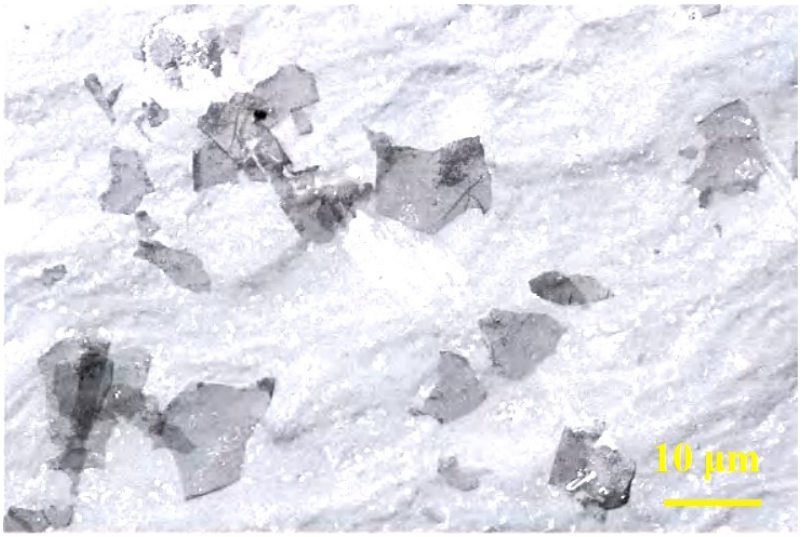

Fig. S6. SEM image of rGA (without NF).

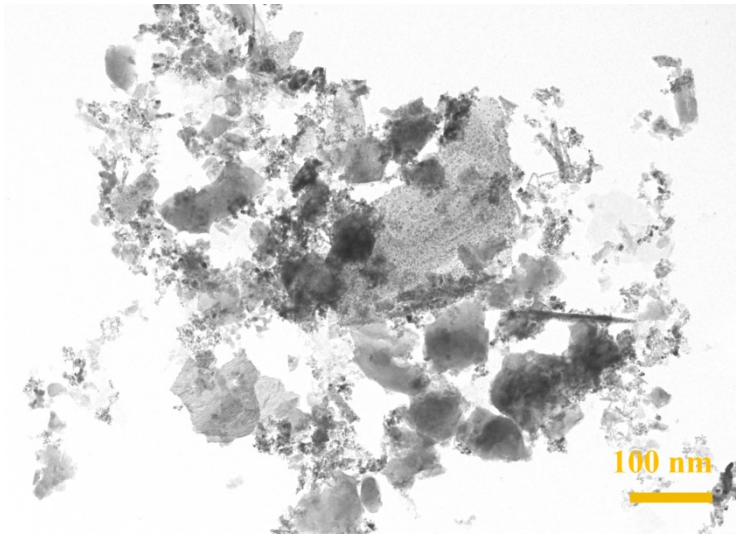

Fig. S7. TEM image of rGA (without NF).

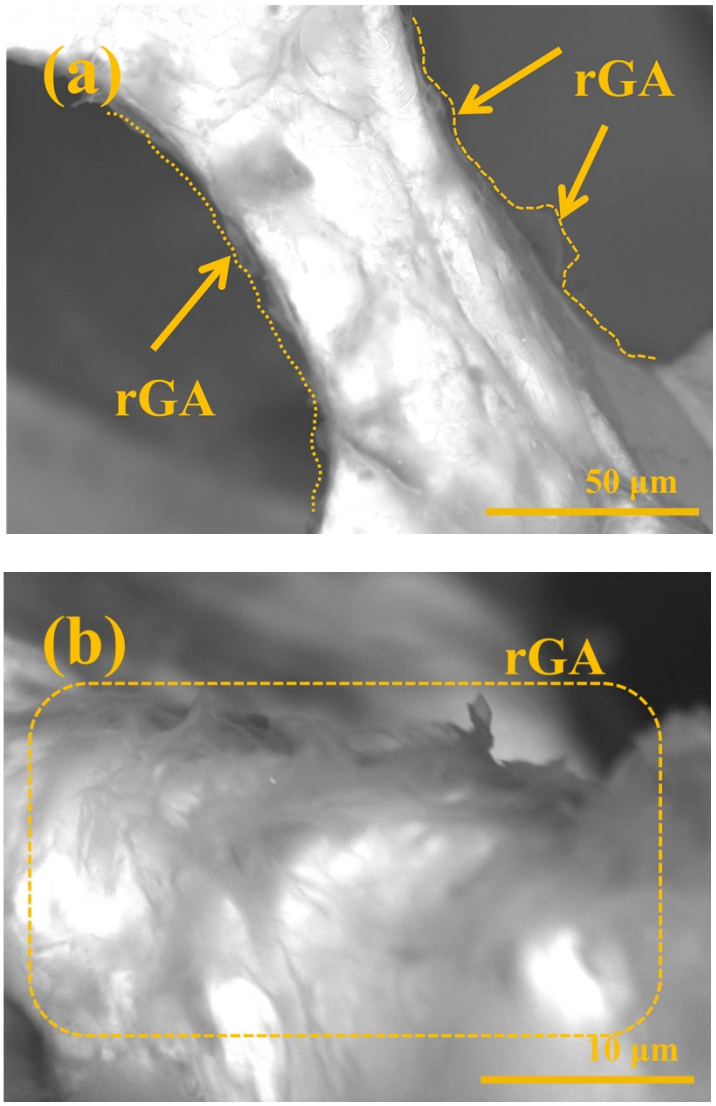

Fig. S8. SEM images of rGA/NF.

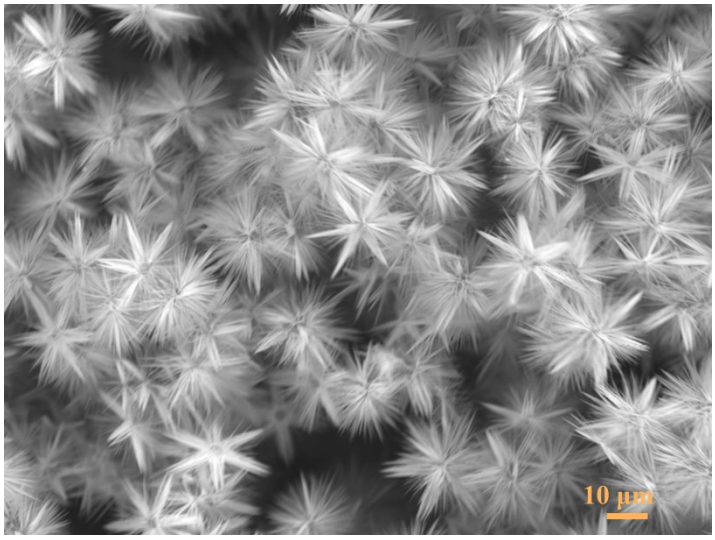

Fig. S9. SEM image of CoP@rGA/NF.

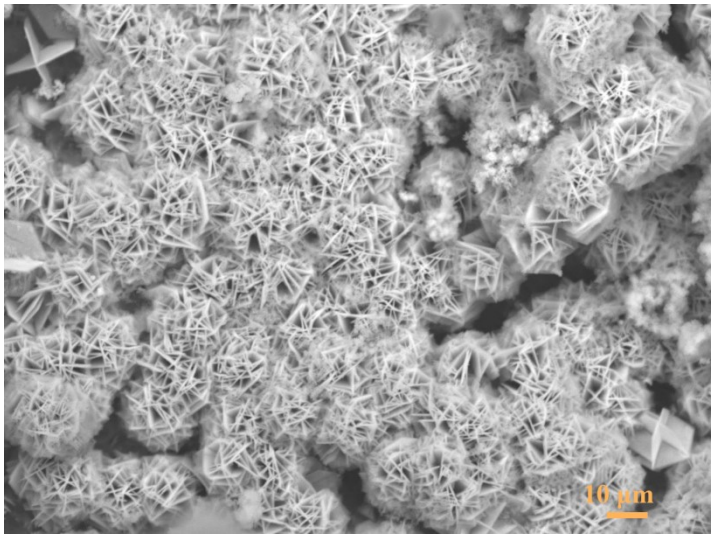

Fig. S10. SEM image of FeP@rGA/NF.

Fig. S11. SEM image of CoCH/NF at 2 µm

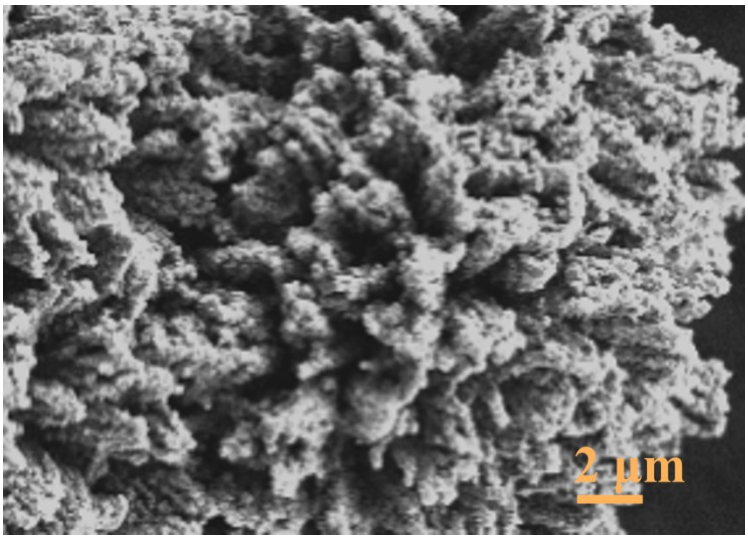

Fig. S12. SEM image of Co-Fe PBA/NF at 2 µm

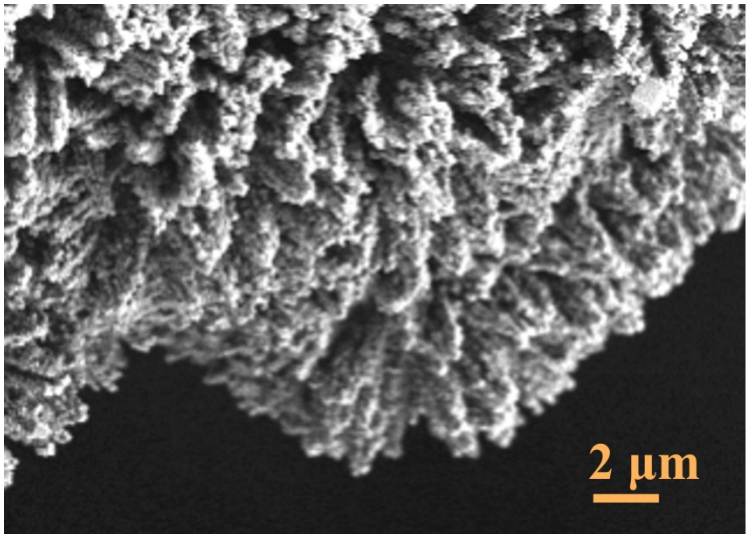

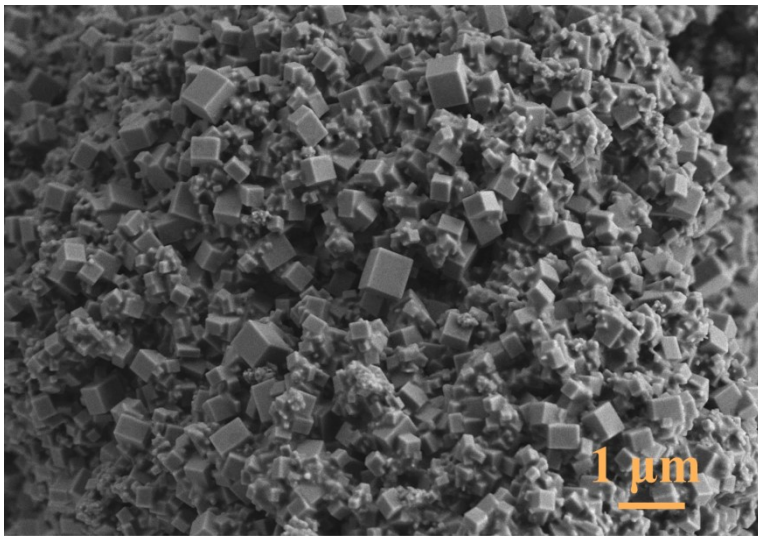

Fig. S13. SEM images of FeP-CoP/NF at 2 μm and 1 μm

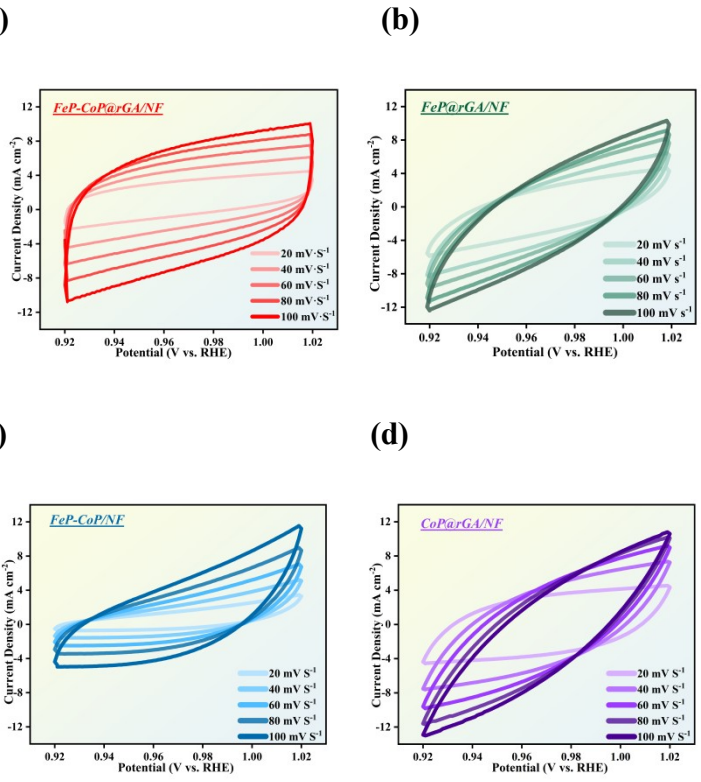

Fig. S14. Cyclic voltammograms of with the non-Faradaic potential regions from 20-100 mV/s for (a) FeP-CoP@rGA/NF, (b) FeP@rGA/NF, (c) FeP-CoP/NF and (d) CoP@rGA/NF.

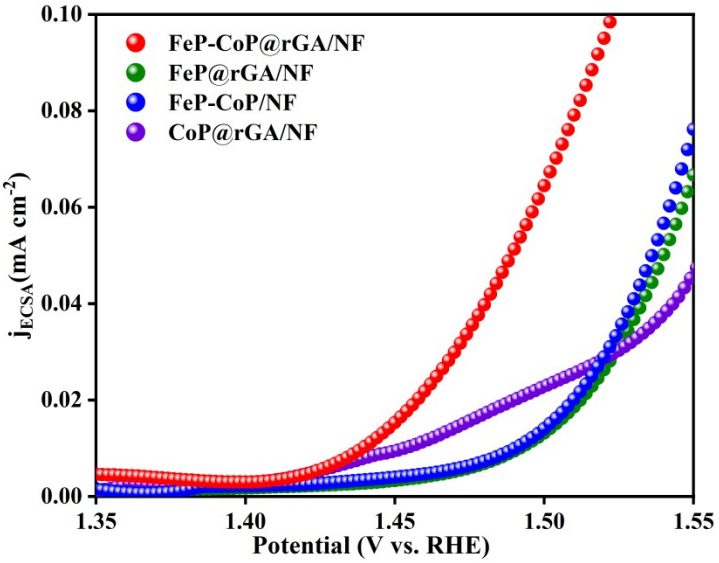

Fig. S15. Polarization curves of different catalysts for OER in 1M KOH electrolyte normalized by ECSA. The specific capacitance (C_s) was chosen as 0.6 mF cm^{-2} in 1 M KOH, based on typical values reported for carbon-based materials (e.g., graphene, carbon nanotubes), owing to their high electric double-layer capacitance. The ECSA of the catalyst layer can be calculated (ECSA = Cdl/Cs).

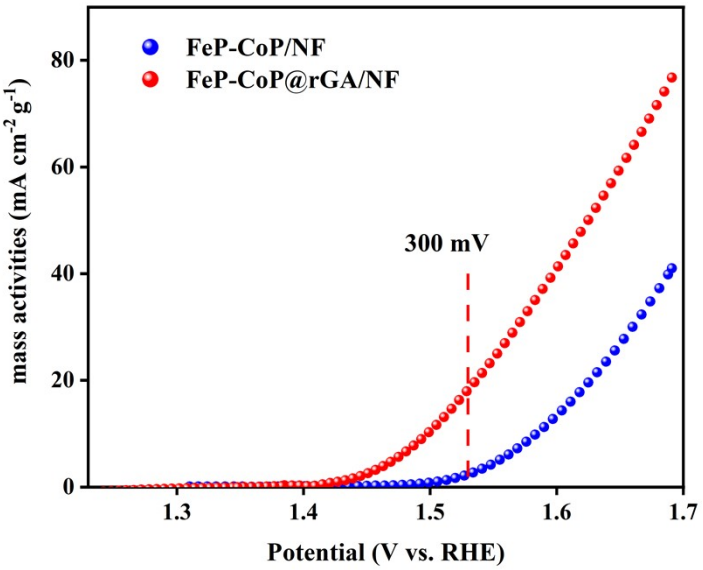

Fig. S16. Mass activities curves of OER derived from LSV curves.

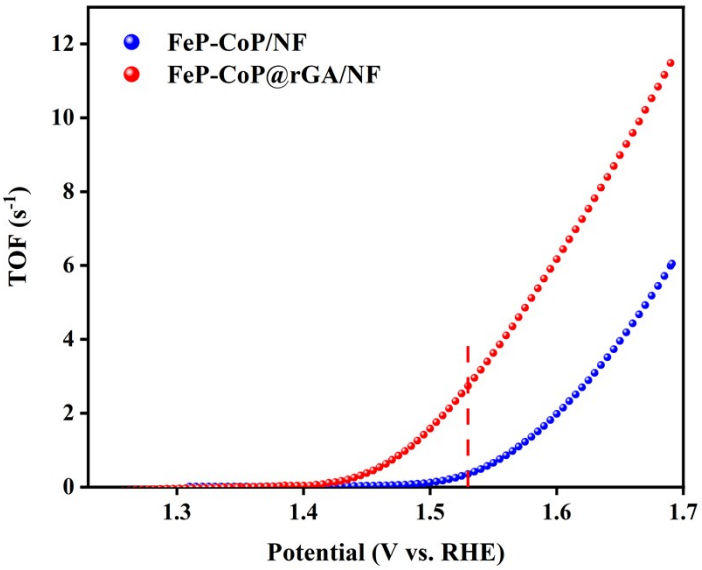

Fig. S17. TOF curves of OER derived from LSV curves.

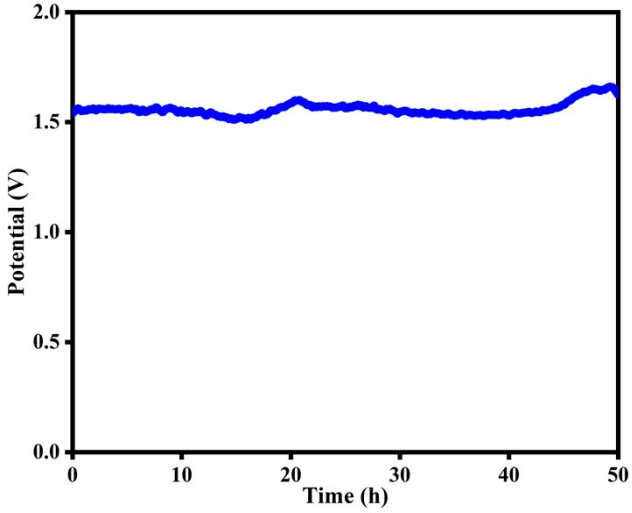

Fig. S18. Chronopotentiometric stability test of FeP-CoP/NF at j = 50 mA cm^{-2} for 50 h.

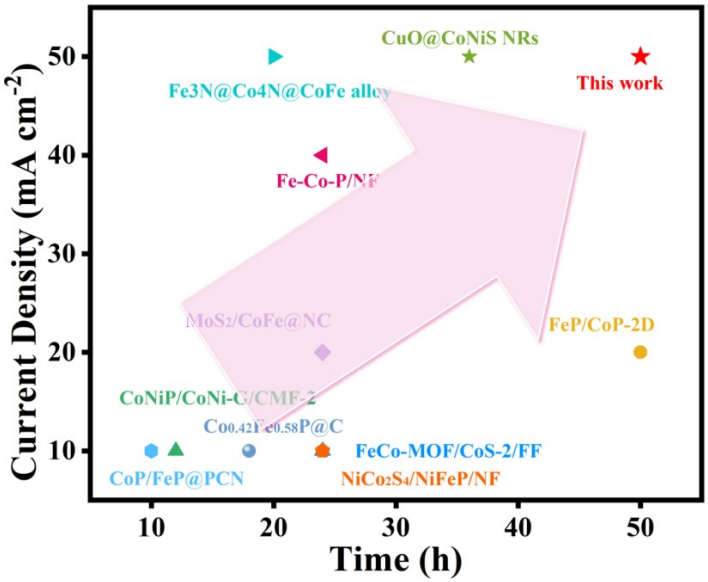

Fig. S19. Comparison of the current density and time for stability between this work and previously reported Fe-Co based catalysts.

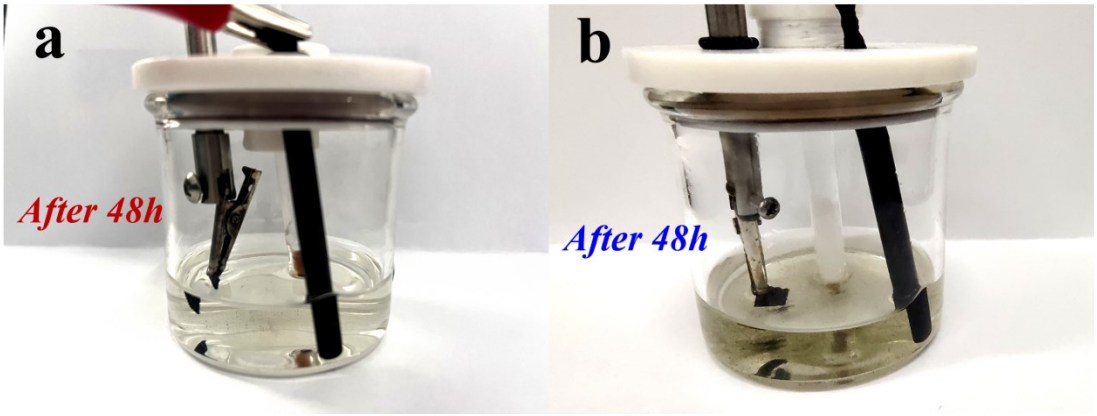

Fig. S20. Comparison of electrolyte conditions after stability test: (a) FeP-CoP@rGA/NF; (b) FeP-CoP/NF.

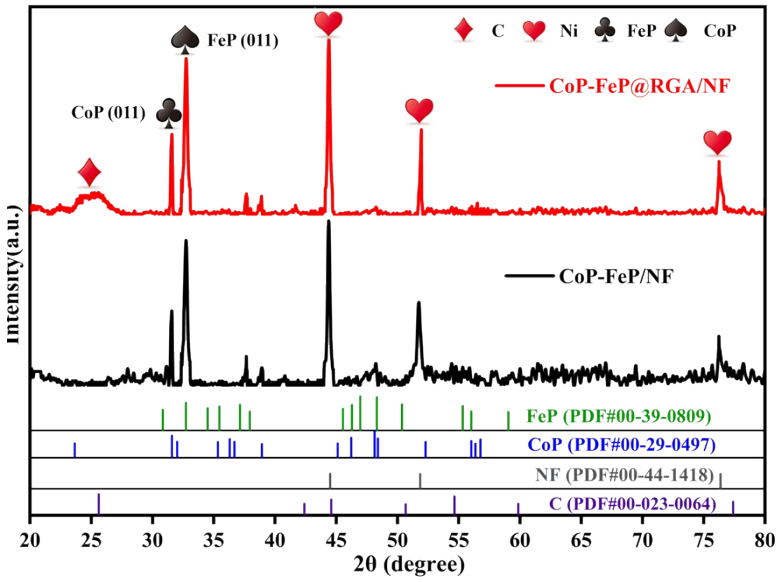

276

277 **Fig. S21.** XRD pattern of FeP-CoP@rGA/NF and FeP-CoP/NF after stability test.

278

279

280

281

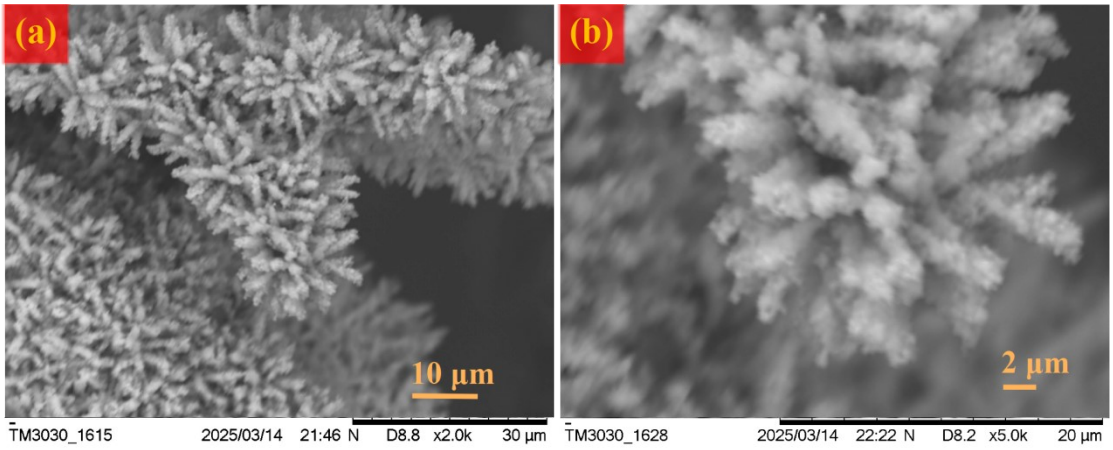

Fig. S22. SEM images of FeP-CoP@rGA/NF after stability test at (a) 10 µm and (b) 2µm.

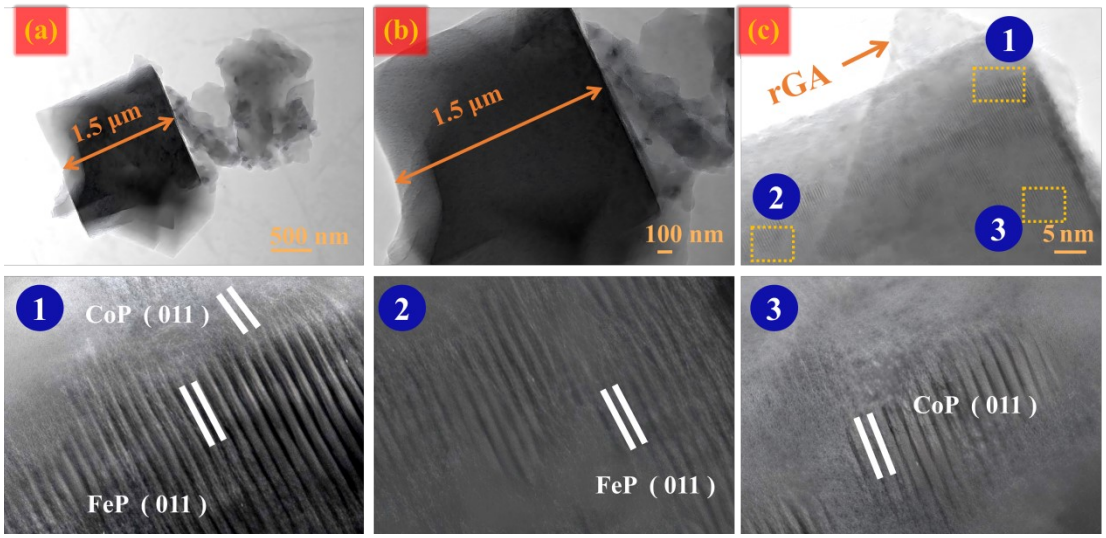

Fig. S23. TEM images of FeP-CoP@rGA/NF after 50h stability test.

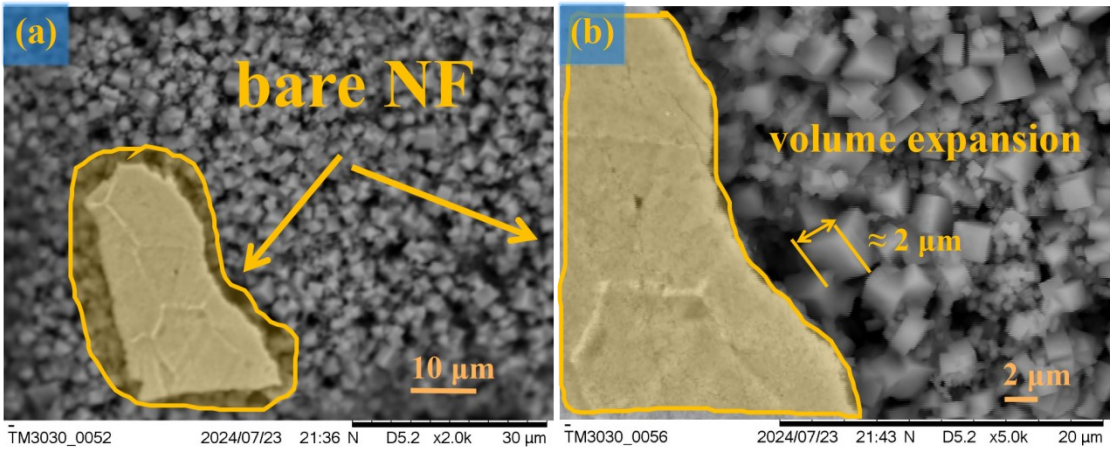

Fig. S24. SEM images of FeP-CoP/NF after stability test at (a) 10 μm and (b) 2μm.

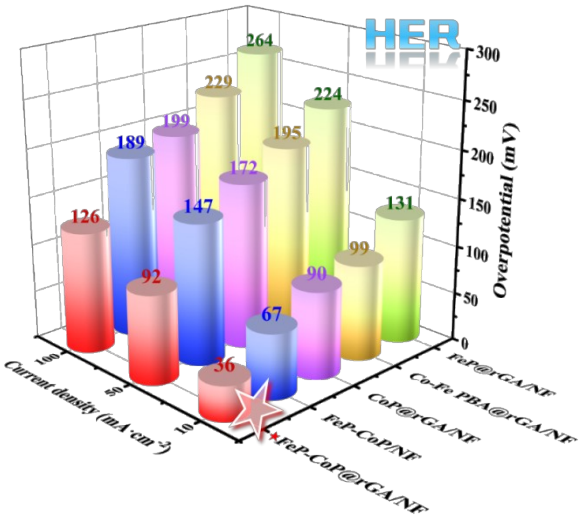

Fig. S25. Catalytic performance comparison of HER.

298 **(a)** **(b)**

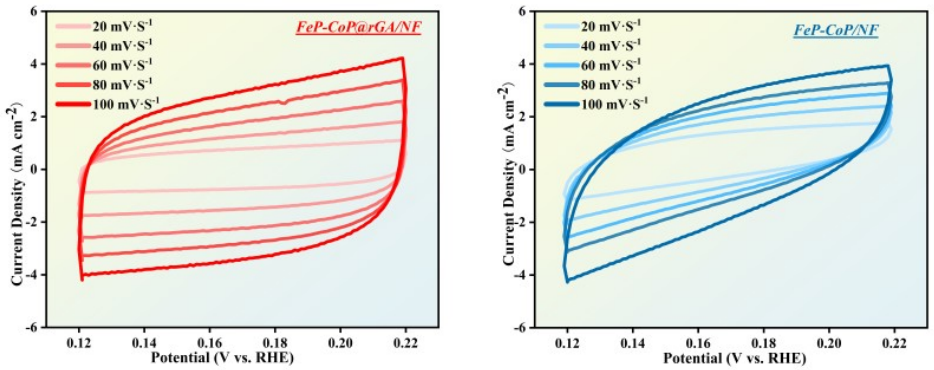

299

300 **(c)** **(d)**

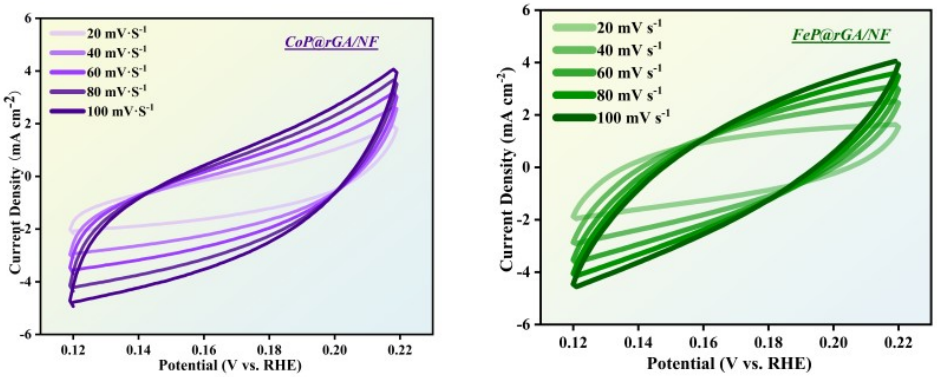

301

302 **Fig. S26.** Cyclic voltammograms of with the non-Faradaic potential regions from 20-

303 100 mV/s for (a) FeP-CoP@rGA/NF, (b) FeP-CoP/NF, (c) CoP@rGA/NF and (d)

304 FeP@rGA/NF.

305

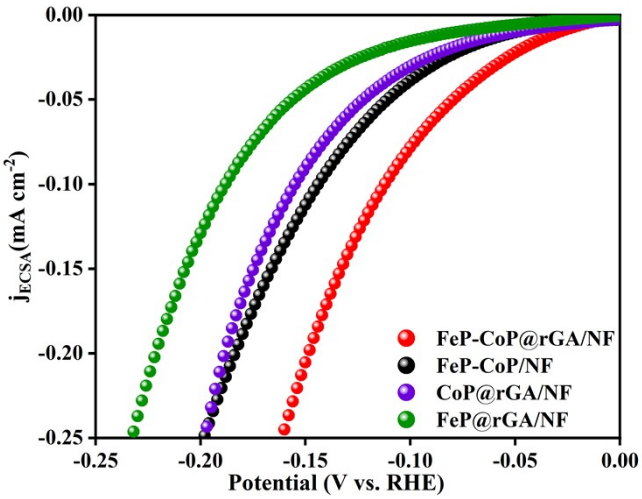

Fig. S27. Polarization curves of different catalysts for HER in 1M KOH electrolyte normalized by ECSA. The specific capacitances (C_S) were chosen as C_S=0.06 mF cm^{-2} in 1 M KOH based on typical reported values. The ECSA of the catalyst layer can be calculated (ECSA = Cdl/Cs).

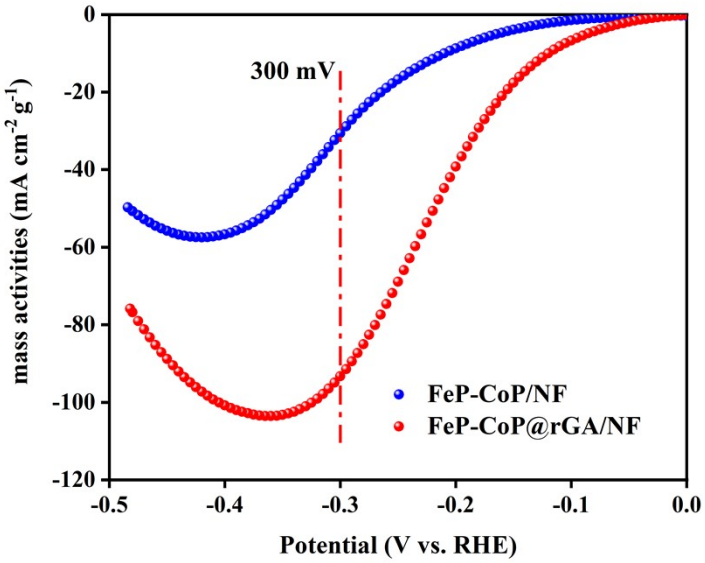

Fig. S28. Mass activities curves of OER derived from LSV curves

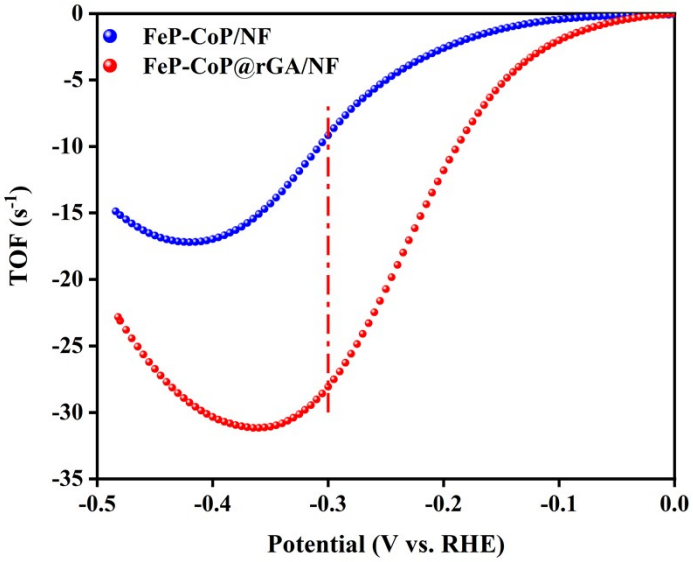

Fig. S29. TOF curves of OER derived from LSV curves.

330
331
332

333 **(a)**

334

335 **(b)**

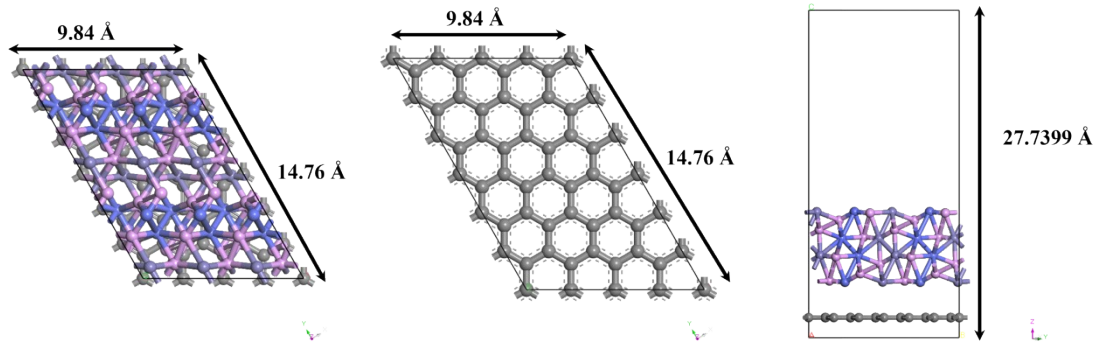

336

337 **Fig. S30.** The theoretical models of DFT. a.FeP-CoP b. FeP-CoP@rGA/NF.

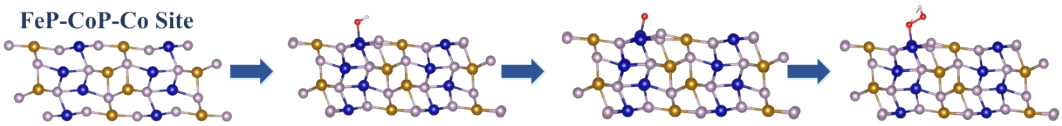

Fig. S31. The configuration of FeP-CoP-Co site(011) adorbs (a) original (b) *OH (c) *O and (d) *OOH.

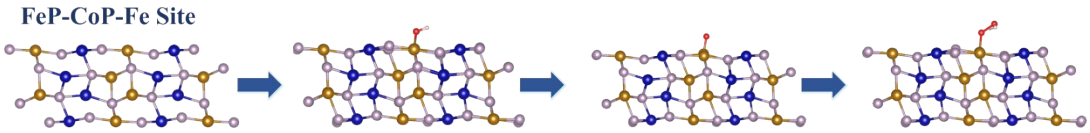

Fig. S32. The configuration of FeP-CoP-Fe site(011) adorbs (a) original (b) *OH (c) *O and (d) *OOH.

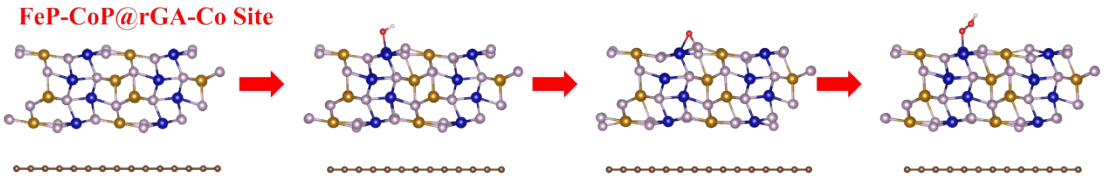

Fig. S33. The configuration of FeP-CoP@rGA-Co site(011) adorbs (a) original (b) *OH (c) *O and (d) *OOH.

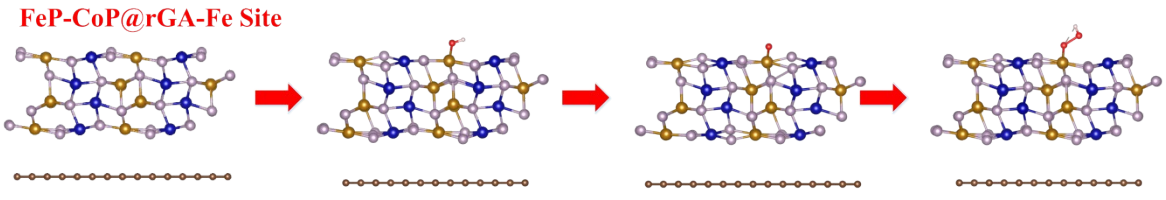

Fig. S34. The configuration of FeP-CoP@rGA-Fe site(011) adorbs (a) original (b) *OH (c) *O and (d) *OOH.

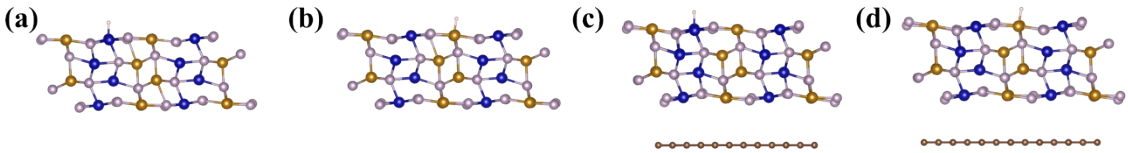

Fig. S35. The configuration of FeP-CoP and FeP-CoP@rGA *H adsorb

FeP-CoP

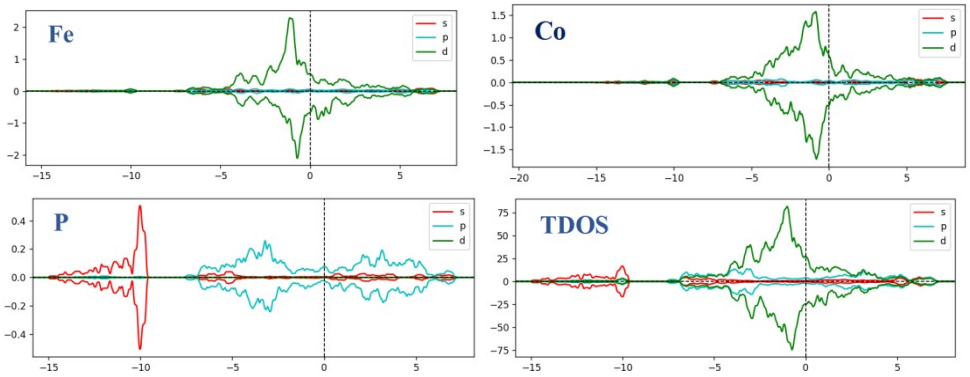

FeP-CoP@rGA

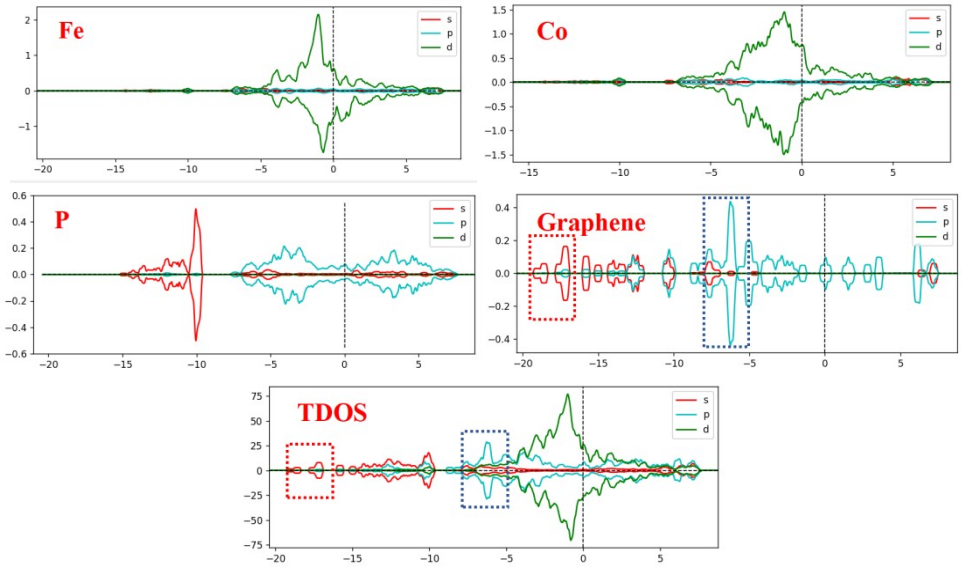

Fig. S36. The DOS of FeP-CoP and FeP-CoP@rGA.

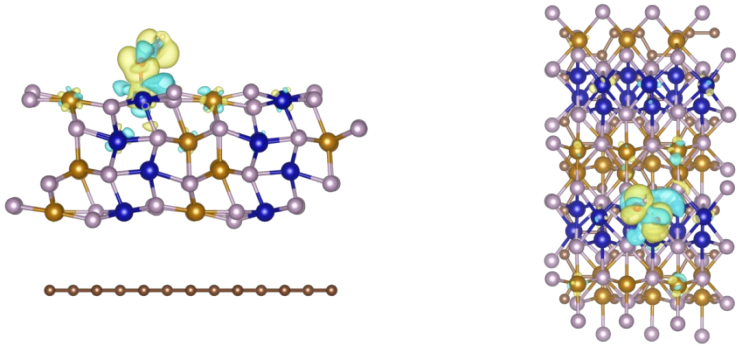

Fig. S37. The charge density difference and Bader of FeP-CoP@rGA on the Co site(*OOH).

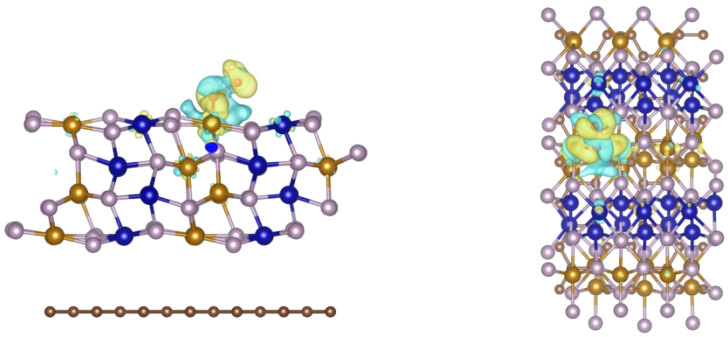

Fig. S38. The charge density difference and Bader of FeP-CoP@rGA on the Fe site(*OOH).

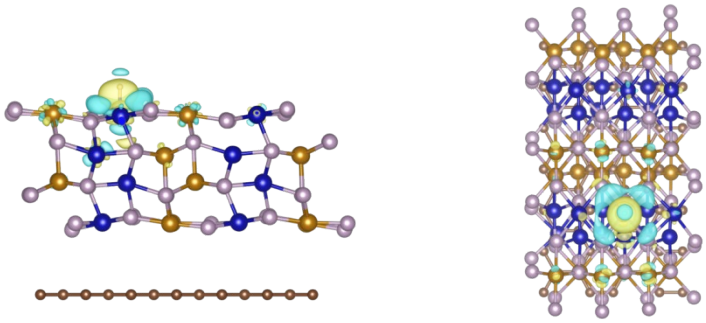

Fig. S39. The charge density difference and Bader of FeP-CoP@rGA on the Co site(*H).

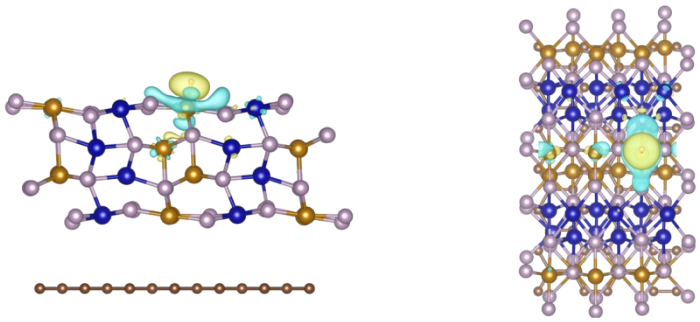

Fig. S40. The charge density difference and Bader of FeP-CoP@rGA on the Fe site(*H).

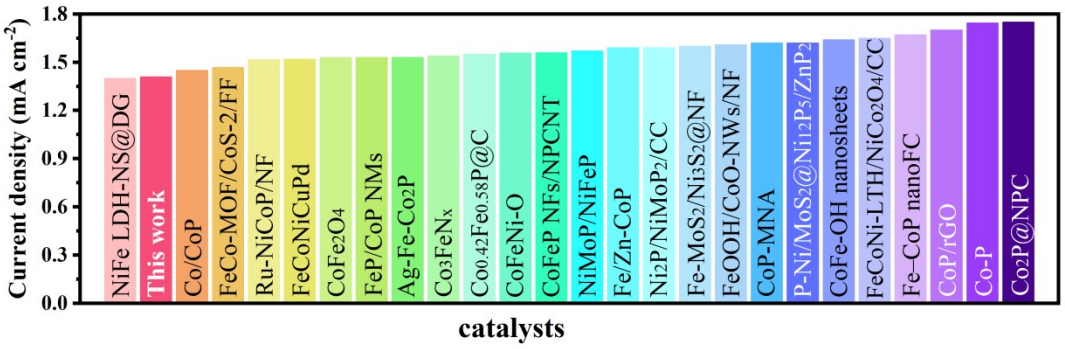

Fig. S41. The voltage of different catalysts for water electrolysis.

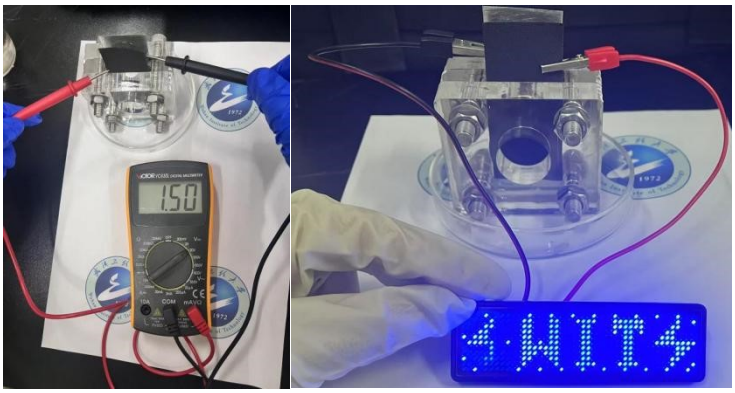

Fig. S42. Digital multimeter measuring the voltage output of zinc-air battery.

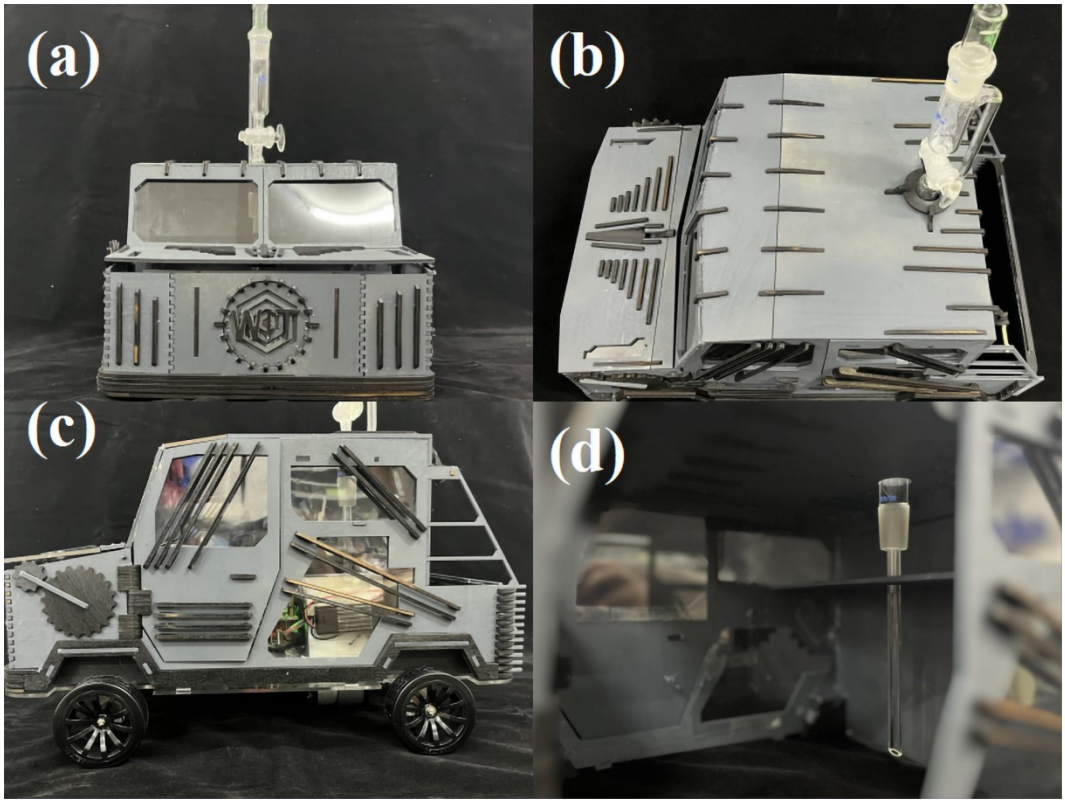

Fig. S43. Structure of the Zn-air battery car: (a) Front view; (b) Top view; (c) Right view; (d) Internal detailed view.

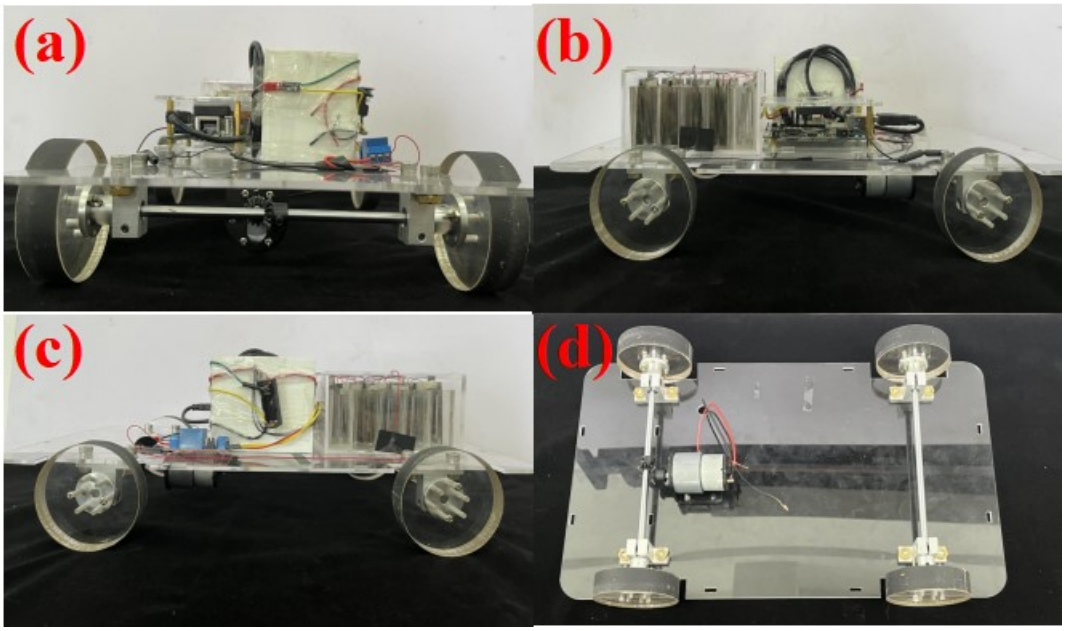

Fig. S44. Internal structure of the zinc-air battery-powered vehicle: (a) Front view, (b) Top view, (c) Right view, (d) Bottom view.

435
436 **Table S1** Mass of the FeP-CoP@rGA (four parallel measurements)

catalyst	Replicate 1 (g)	Replicate 2 (g)	Replicate 3 (g)	Replicate 4 (g)	Average (g)
NF	0.0708	0.0691	0.0699	0.0699	0.0699
rGA/NF	0.0864	0.0833	0.0851	0.0849	0.0849
FeP-CoP@rGA/NF	0.1807	0.1769	0.1792	0.1789	0.1789
FeP-CoP@rGA	0.1099	0.1078	0.1093	0.1090	0.1090

438 **Table S2** Mass of the FeP-CoP catalyst on NF (four parallel measurements)
439

catalyst	Replicate 1 (g)	Replicate 2 (g)	Replicate 3 (g)	Replicate 4 (g)	Average (g)
NF	0.0698	0.0691	0.0697	0.0699	0.0696
FeP-CoP/NF	0.1851	0.1843	0.1851	0.1849	0.1849
FeP-CoP	0.1153	0.1152	0.1154	0.1150	0.1152

Table S3 Co and Fe mass of the FeP-CoP@rGA obtained from ICP-OES measurements

FeP-CoP@rGA	Fe (mg)	Co (mg)	(Fe+Co) (mg)	(Fe+Co) wt%
m1	1.78	2.31	4.09	40.5
m2	1.74	2.28	4.02	40.2
m3	1.76	2.29	4.05	40.5
m3	1.76	2.28	4.04	40.4
average	**1.76**	**2.29**	**4.05**	**40.5**

443 **Table S4** Co and Fe mass of the FeP-CoP obtained from ICP-OES measurements
444

FeP-CoP	Fe (mg)	Co (mg)	(Fe+Co) (mg)	(Fe+Co) wt%
m1	2.98	3.04	6.02	60.2
m2	2.77	2.94	5.71	57.1
m3	2.88	2.95	5.81	58.1
M4	2.88	3.01	5.91	59.1
average	**2.88**	**2.99**	**5.87**	**58.7**

445
446 **Table S5**. The ECSA of different samples in OER and HER.

Num.	catalyst	OER (cm^2)	HER (cm^2)
1	FeP-CoP@rGA/NF	1055	505
2	FeP-CoP/NF	518.33	301.67
3	FeP@rGA/NF	673.33	256.67
4	CoP@rGA/NF	283.33	148.33

448 **Table S6**. At 50 mA cm^{-2}, comparison of stability duration for iron-cobalt-based
449 catalysts in recent years.
450
451

Num.	catalyst	Time (h)	Current Density (mA cm^{-2})	Ref.
1	FeP-CoP@rGA/NF	50	50	This work
2	FeP/CoP-2D	50	20	2
3	FeCo-MOF/CoS-2/FF	24	10	3
4	CoNiP/CoNi-G/CMF-2	12	10	4
5	MoS_2/CoFe@NC	24	20	5
6	Fe-Co-P/NF	24	40	6
7	Fe_3N@Co_4N@CoFe alloy	20	50	7
8	CoP/FeP@PCN	10	10	8
9	CuO@CoNiS NRs	36	50	9
10	$NiCo_2S_4$/NiFeP/NF	24	10	10
11	$Co_{0.42}Fe_{0.58}P$@C	18	10	11

452

Table S7. At 50 mA cm^{-2}, comparison of OER and HER performance of Fe-Co based catalysts in recent years.

Num.	Catalysts	HER Overpotential @ j (mV @ 50mA cm^{-2}) ≈	OER Overpotential @ j (mV @ 50 mA cm^{-2}) ≈	Electrolyte	Ref.
1	FeP-CoP@rGA/NF	191	210	1M KOH	This work
2	Mo-Co-Fe-MOF	317	296	1M KOH	12
3	CoFeZr/NF	248	267	1M KOH	13
4	$Cu_{0.50}Fe_{0.50}$/NF	234	270	1M KOH	14
5	$Co_{0.42}Fe_{0.58}P$@C	229	302	1M KOH	11
6	CoFe@N-C-700°C	204	348	1M KOH	15
7	FeNi LDH/V_2CT_x/NF	274	265	1M KOH	16
8	CoNiP/CoNi-G/CMF-2	290	385	1M KOH	4
9	MoS_2/CoFe@NC	331	406	1M KOH	5
10	Fe-CoP nanoFC	347	320	1M KOH	17
11	S-NiFe/NFF	285	213	1M KOH	18
12	FeS_2/FeOOH@NF	253	283	1M KOH	19
13	$Ni_5P_4/Ni_2P/Fe_2P$-2	223	263	1M KOH	20
14	FeOOH/CoO-NWs/NF	202	249	1M KOH	21
15	MoS_2@CoO	274	396	1M KOH	22

458 **Table S8** Lattice parameters and Angle in the calculation.

	Lattice parameter	Angle
FeP-CoP@rGA (011)	14.76×9.84×27.74 Å;	a = b = c = 90°
FeP-CoP (011)	14.76×9.84×27.74 Å;	a = b = c = 90°

459

460 **Table S9** Computational Parameters for DFT Geometry Optimization.

Parameter	Value	Description
Software	VASP	Vienna Ab initio Simulation Package
Functional	GGA-PBE	Perdew-Burke-Ernzerhof exchange-correlation functional
Pseudopotential	PAW	Projector Augmented-Wave
Cutoff Energy (ENCUT)	400 eV	Plane-wave basis set kinetic energy cutoff
k-point	1×1×1	Used for the large supercell model
SCF Convergence (EDIFF)	1×10^{-5}	Energy tolerance for electronic loop
Force Convergence (EDIFFG)	-0.01 eV/Å	Force tolerance on all atoms for ionic relaxation
Smearing Method (ISMEAR)	0	
Smearing Width (SIGMA)	0.05	
Algorithm (IBRION)	2	Conjugate gradient algorithm for ionic relaxation

461

462 **Table S10** Computational Parameters for DFT Static Self-Consistent Field

463 Calculations.

Category	Parameter	Value / Setting	Description
Basic Setup	Functional	GGA-PBE	Exchange-correlation functional
	Pseudopotential	PAW	Projector Augmented-Wave method
	ENCUT	400 eV	Cut-off energy for plane wave basis set, in eV
	PREC	Accurate	(Precision level: Normal or Accurate, set Accurate when perform structure lattice relaxation calculation)
SCF Convergence	EDIFF	1×10^{-8} eV	SCF energy convergence, in eV
	NELM	60	Maximum number of electronic steps
DOS Calculation	k-mesh Sampling	3×3×1	KPOINTS
	ISMEAR	-5	gaussian smearing method
	LORBIT	11	Enables projected DOS (PDOS) output
	NEDOS	2001	DOSCAR points
I/O Settings	ISTART	1	Read existing WAVECAR
	ICHARG	2	Non-self-consistent: GGA/LDA band structures

464

Table S11. Energy values for H_2O, O_2 and H_2.

	Pressure (bar)	E_{DFT} (eV)	ZPE (eV)	G (eV)	Temperature (k)
O_2(g)	1	–	–	-9.900	298.15
H_2(g)	1	-6.760	-0.045	-6.818	298.15
H_2O(l)	0.035	-14.223	-0.000	-14.228	298.15

Table S12. The values used for zero-point energy corrections (eV).

	Different sites	zero-point energy correction value
*H	FeP-CoP Fe site	0.166707
*H	FeP-CoP Co site	0.170521
*H	FeP-CoP@rGA Fe site	0.163666
*H	FeP-CoP@rGA Co site	0.170034

Table S13. Adsorption free energies of *H (eV) on different sites of FeP-CoP(011), FeP-CoP@rGA(011) surface.

Different sites	ΔGH
FeP-CoP Fe site	-1.16
FeP-CoP Co site	-0.61
FeP-CoP@rGA Fe site	-1.13
FeP-CoP@rGA Co site	-0.47

Yellow marked sites are the active sites on each surface.

Table S14. Adsorption free energies of *OH, *O and *OOH (eV) on the active site of FeP-CoP(011), FeP-CoP@rGA(011) surface.

	ΔG_{*OH}	ΔG_{*O}	ΔG_{*OOH}
FeP-CoP Fe site	-0.361	0.266	2.908
FeP-CoP Co site	1.295	0.917	4.143
FeP-CoP@rGA Fe site	-0.753	0.995	2.476
FeP-CoP@rGA Co site	0.685	2.074	3.652

Table S15. The water splitting activity of FeP-CoP@rGA/NF and other bifunctional OER/HER Catalysts based on Fe-Co in alkaline electrolyte.

Num.	catalyst	electrolyte	cell voltage (V) (10 mA cm^{-2})	Ref.
1	FeP/CoP@rGA/NF	1M KOH	1.41	This work
2	NiFe LDH-NS@DG	1M KOH	~1.4	23
3	Co/CoP	1M KOH	1.45	24
4	FeCo-MOF/CoS-2/FF	1M KOH	1.468	3
5	Ru-NiCoP/NF	1M KOH	1.515	25
6	FeCoNiCuPd	1M KOH	1.52	26
7	$CoFe_2O_4$	1M KOH	1.53	27
8	FeP/CoP NMs	1M KOH	1.53	28
9	Ag-Fe-Co_2P	1M KOH	1.53@100	29
10	Co_3FeN_x	1M KOH	1.539	30
11	$Co_{0.42}Fe_{0.58}P$@C	1M KOH	1.55	11
12	CoFeNi-O	1M KOH	1.558	31
13	CoFeP NFs/NPCNT	1M KOH	1.56	32
14	NiMoP/NiFeP	1M KOH	1.57	33
15	Fe/Zn-CoP	1M KOH	1.59	34
16	$Ni_2P/NiMoP_2$/CC	1M KOH	1.59	35
17	Fe-MoS_2/Ni_3S_2@NF	1M KOH	1.60	36
18	FeOOH/CoO-NWs/NF	1M KOH	1.61	21
19	CoP-MNA	1M KOH	1.62	37
20	P-Ni/MoS_2@$Ni_{12}P_5/ZnP_2$	1M KOH	1.62@50	38
21	CoFe-OH nanosheets	1M KOH	1.64	39
22	FeCoNi-LTH/$NiCo_2O_4$/CC	1M KOH	1.65@50	40
23	Fe–CoP nanoFC	1M KOH	1.671	17

24	CoP/rGO	1M KOH	1.7	41
25	Co-P	1M KOH	1.744@100	42
26	Co_2P@NPC	1M KOH	1.75	43

491

Table S16. The Specifications of GO (H_2O wt% ≤6)

	Tap density	pH 1% concentration	C(wt%) Elementanalysis	Particle Size D50（μm) laserparticle analyzer
GO	0.7-1.2	1.6-2.6	45-55	15-30

498

References

1 X. Ma, Y. Zhou, S. Zhang, W. Lei, Y. Zhao, C. Shan, 3d – 5d Orbital Hybridization in Nanoflower - Like High - Entropy Alloy for Highly Efficient Overall Water Splitting at High Current Density, Small 21 (2025) 2411394. https://doi.org/10.1002/smll.202411394.

2 S. Fu, C. Peng, Y. Luo, L. Cheng, X. Yang, Z. Jiao, Modulating space charge of FeP/CoP p-n heterojunction for boosting oxygen evolution reaction, J. Colloid Interface Sci. (2024). https://doi.org/10.1016/j.jcis.2024.03.060.

3 Y. Xu, Q. Zhang, N. Wang, L. Huang, X. Zhang, H. Lin, Y. Xu, J. Chen, Y. Jiao, Quasi-FeCo-MOF/CoS amorphous Nanosheets: A stable and highly active catalyst for electrocatalytic water splitting and monosaccharide oxidation, Chem. Eng. J. 497 (2024) 154837. https://doi.org/10.1016/j.cej.2024.154837.

4 D. Wei, L. Chen, L. Tian, S. Ramakrishna, D. Ji, Hierarchically Structured CoNiP/CoNi Nanoparticle/Graphene/Carbon Foams as Effective Bifunctional Electrocatalysts for HER and OER, Ind. Eng. Chem. Res. 62 (2023) 4987-4994. https://doi.org/10.1021/acs.iecr.3c00224.

5 W. Ma, W. Li, H. Zhang, Y. Wang, N-doped carbon wrapped CoFe alloy nanoparticles with MoS_2 nanosheets as electrocatalyst for hydrogen and oxygen evolution reactions, Int. J. Hydrogen Energy. 48 (2023) 22032-22043. https://doi.org/10.1016/j.ijhydene.2023.03.095.

6 H. Xu, J. Zhu, P. Wang, D. Chen, C. Zhang, M. Xiao, Q. Ma, H. Bai, R. Qin, J. Ma, S. Mu, Fe-Co-P multi-heterostructure arrays for efficient electrocatalytic water splitting, J. Mater. Chem. A. (2021). https://doi.org/10.1039/d1ta06603j.

7 C. Zihao, L. Xizhuang, W. Peng, Z. Peng, Z. Qianqian, W. Zeyan, Z. Zhaoke, L. Yuanyuan, D. Ying, H. Baibiao, In situ integration of Fe_3N@Co_4N@CoFe alloy nanoparticles as efficient and stable electrocatalyst for overall water splitting,

Electrochim. Acta. 395 (2021) 139218. https://doi.org/10.1016/j.electacta.2021.139218.

8 K. Chen, L. Wang, J. Long, F. Zhao, L. Kang, Petaloid CoP/FeP Composites: Efficiently bifunctional cathode electrochemical oxygen catalysts for aqueous and Solid-State Zinc-Air batteries, Chem. Eng. J. 496 (2024) 153820. https://doi.org/10.1016/j.cej.2024.153820.

9 Y. Jiangtao, X. Haicheng, Z. Guohong, W. Rui, Y. Jiale, L. Xiaohong, L. Yuping, H. Peide, The 3D core-shell heterostructure catalysts by CoNiS nanosheets interfacial assembled on CuO nanorods for efficient water electrolysis, Appl. Surf. Sci. 570 (2021) 151181. https://doi.org/10.1016/j.apsusc.2021.151181.

10 J. Jing, L. Fengyan, S. Hui, G. Yangqin, L. Ning, G. Lei, Flower-like $NiCo_2S_4$/NiFeP/NF composite material as an effective electrocatalyst with high overall water splitting performance, Chin. Chem. Lett. 33 (2021) 4367-4374. https://doi.org/10.1016/j.cclet.2021.12.028.

11 Y. Deng, Y. Cao, Y. Xia, X. Xi, Y. Wang, W. Jiang, D. Yang, A. Dong, T. Li, Self-Templated Synthesis of CoFeP@C Cage-In-Cage Superlattices for Enhanced Electrocatalytic Water Splitting, Adv. Energy Mater. (2022) https://doi.org/10.1002/aenm.202202394.

12 Y. Hai, X. Shengquan, Y. Jiawei, L. Jianguo, T. Wei, Y. Jianfei, W. Junyi, Z. Min, W. Congrong, Z. Miao, H. Gang, Y. Lei, Co_3Fe_7/Mo_2C co-embedded in N-codoped porous carbon with accelerated kinetics for OER and HER, Colloids Surf. A. 645 (2022)128953. https://doi.org/10.1016/j.colsurfa.2022.128953.

13 W. Liu, K. Jiang, Y. Hu, Q. Li, Y. Deng, J. Bao, Y. Lei, Zr-doped CoFe-Layered Double Hydroxides for highly efficient seawater electrolysis, J. Colloid Interface Sci. 604 (2021) 767-775. https://doi.org/10.1016/j.jcis.2021.07.022

14 A.I. Inamdar, H.S. Chavan, B. Hou, C.H. Lee, S.U. Lee, S. Cha, H. Kim, H. Im, A Robust Nonprecious CuFe Composite as a Highly Efficient Bifunctional Catalyst for Overall Electrochemical Water Splitting, Small. 16 (2019) 1905884. https://doi.org/10.1002/smll.201905884.

15 X. Zeng, M.J. Jang, S.M. Choi, H.-S. Cho, C.-H. Kim, N.V. Myung, Y. Yin, Single-crystalline CoFe nanoparticles encapsulated in N-doped carbon nanotubes as a bifunctional catalyst for water splitting, Mater. Chem. Front. 4 (2020) 2307-2313. https://doi.org/10.1039/d0qm00126k.

16 L. Y ang, T. Yang, Y. Chen, Y. Zheng, E. Wang, Z. Du, K.-C. Chou, X. Hou, FeNi LDH/V_2CT_x/NF as self-supported bifunctional electrocatalyst for highly effective overall water splitting, Nanomaterials 12 (2022) 2640. https://doi.org/10.3390/nano12152640.

17 Y. Yuan, Y. Yang, H. Xie, X. Zhong, R. Wang, Z. Xu, Trace Fe doping improved the OER and HER catalytic performance of CoP hollow nanoflower clusters, Int. J. Hydrogen Energy 90 (2024) 1401–1410. https://doi.org/10.1016/j.ijhydene.2024.10.122.

18 L. Wu, J. Feng, Z. Zou, K. Song, C. Zeng, Formation of feathery-shaped dual-function S-doped FeNi-MOFs to achieve advanced electrocatalytic activity for OER and HER, J. Electroanal. Chem. 935 (2023) 117365. https://doi.org/10.1016/j.jelechem.2023.117365.

19 Y. Yang, Y. Chen, Y. Xiong, Y. He, Q. Sun, D. Xu, Z. Hu, Self-supported monometallic FeS_2/FeOOH-ZnO@NF with abundant oxygen vacancies as efficient and stable electrocatalysts for the OER and HER, J. Alloys Compd. 991 (2024) 174525. https://doi.org/10.1016/j.jallcom.2024.174525.

20 S. Sun, C. Zhang, M. Ran, Y. Zheng, C. Li, Y. Jiang, X. Yan, Fe-doped promotes phosphorization and dispersibility of Ni catalysts for efficient and stable HER and

OER, Int. J. Hydrogen Energy 63 (2024) 133-141. https://doi.org/10.1016/j.ijhydene.2024.03.179.

21 H. Zhang, W. Li, X. Feng, N. Chen, H. Zhang, X. Zhao, L. Wang, Z. Li, Interfacial FeOOH/CoO nanowires array improves electrocatalytic water splitting, J. Solid State Chem. 298 (2021) 122156. https://doi.org/10.1016/j.jssc.2021.122156.

22 P. Cheng, C. Yuan, Q. Zhou, X. Hu, J. Li, X. Lin, X. Wang, M. Jin, L. Shui, X. Gao, R. Nötzel, G. Zhou, Z. Zhang, J. Liu, Core-shell MoS_2@CoO electrocatalyst for water splitting in neural and alkaline solutions, J. Phys. Chem. C 123 (2019) 5833-5839. https://doi.org/10.1021/acs.jpcc.8b10954.

23 Y. Jia, L. Zhang, G. Gao, H. Chen, B. Wang, J. Zhou, M.T. Soo, M. Hong, X. Yan, G. Qian, J. Zou, A. Du, X. Yao, A heterostructure coupling of exfoliated Ni-Fe hydroxide nanosheet and defective graphene as a bifunctional electrocatalyst for overall water splitting, Adv. Mater. 29 (2017) 1700017. https://doi.org/10.1002/adma.201700017.

24 J. Lin, Y. Yan, T. Liu, J. Cao, X. Zhou, J. Feng, J. Qi, Optimize the electrocatalytic performances of NiCoP for water splitting by the synergic effect of S dopant and P vacancy, Int. J. Hydrogen Energy 45 (2020) 16161-16168. https://doi.org/10.1016/j.ijhydene.2020.04.069.

25 D. Chen, R. Lu, Z. Pu, J. Zhu, H.-W. Li, F. Liu, S. Hu, X. Luo, J. Wu, Y. Zhao, S. Mu, Ru-doped 3D flower-like bimetallic phosphide with a climbing effect on overall water splitting, Appl. Catal., B 279 (2020) 119396. https://doi.org/10.1016/j.apcatb.2020.119396.

26 S. Wang, B. Xu, W. Huo, H. Feng, X. Zhou, F. Fang, Z. Xie, J.K. Shang, J. Jiang, Efficient FeCoNiCuPd thin-film electrocatalyst for alkaline oxygen and hydrogen evolution reactions, Appl. Catal., B 313 (2022) 121472. https://doi.org/10.1016/j.apcatb.2022.121472.

603 27 C. Guo, X. Liu, L. Gao, X. Ma, M. Zhao, J. Zhou, X. Kuang, W. Deng, X. Sun, Q.
604 Wei, Oxygen defect engineering in cobalt iron oxide nanosheets for promoted overall
605 water splitting, J. Mater. Chem. A 7 (2019) 21704-21710.
606 https://doi.org/10.1039/C9TA06537G.
607 28 Y. Du, L. Zhan, Y. Liu, R. Chen, Y. Fu, B. Li, L. Wang, Morphology engineering
608 induces the increase of FeP/CoP heterointerface density for efficient alkaline water
609 splitting driven by interfacial dual active sites, Mater. Chem. Front. 7 (2023) 4573-
610 4583. https://doi.org/10.1039/D3QM00489A.
611 29 K.-L. Yan, X. Shang, L.-M. Zhang, B. Dong, Z.-Z. Liu, J.-Q. Chi, W.-K. Gao, Y.-
612 M. Chai, C.-G. Liu, Boosting electrocatalytic activity of binary ag-e-doped co 2 P
613 nanospheres as bifunctional electrocatalysts for overall water splitting, Electrochim.
614 Acta 249 (2017) 16-25. https://doi.org/10.1016/j.electacta.2017.07.180.
615 30 Y. Wang, D. Liu, Z. Liu, C. Xie, J. Huo, S. Wang, Porous cobalt–iron nitride
616 nanowires as excellent bifunctional electrocatalysts for overall water splitting, Chem.
617 Commun. 52 (2016) 12614-12617. https://doi.org/10.1039/C6CC06608A.
618 31 L. Han, L. Guo, C. Dong, C. Zhang, H. Gao, J. Niu, Z. Peng, Z. Zhang, Ternary
619 mesoporous cobalt-iron-nickel oxide efficiently catalyzing oxygen/hydrogen
620 evolution reactions and overall water splitting, Nano Res. 12 (2019) 2281-2287.
621 https://doi.org/10.1007/s12274-019-2389-5.
622 32 W. Li, Y. Chen, B. Yu, Y. Hu, X. Wang, D. Yang, 3D hollow Co-Fe-P nanoframes
623 immobilized on N, P-doped CNT as an efficient electrocatalyst for overall water
624 splitting, Nanoscale 11 (2019) 17031-17040. https://doi.org/10.1039/C9NR05924E.
625 33 H. Roh, H. Jung, H. Choi, J.W. Han, T. Park, S. Kim, K. Yong, Various metal (Fe,
626 Mo, V, co)-doped Ni_2P nanowire arrays as overall water splitting electrocatalysts and
627 their applications in unassisted solar hydrogen production with STH 14 %, Appl.
628 Catal., B 297 (2021) 120434. https://doi.org/10.1016/j.apcatb.2021.120434.

34 P. Wang, X. Liu, Y. Yan, J. Cao, J. Feng, J. Qi, Exploring CoP core-shell nanosheets by Fe and Zn dual cation doping as efficient electrocatalysts for overall water splitting, Catal. Sci. Technol. 10 (2020) 1395-1400. https://doi.org/10.1039/C9CY02425E.

35 L. Sun, S. Zhao, L. Sha, G. Zhuang, X. Wang, X. Han, Self-supported $Ni_2P/NiMoP_2$ bimetallic phosphide with strong electronic interaction for efficient overall water splitting, J. Colloid Interface Sci. 637 (2023) 76-84. https://doi.org/10.1016/j.jcis.2023.01.035.

36 T. Wang, B. Li, P. Wang, M. Xu, D. Wang, Y. Wang, W. Zhang, C. Qu, M. Feng, Modulation of electronic structure of Ni_3S_2 via Fe and Mo co-doping to enhance the bifunctional electrocatalytic activities for HER and OER, J. Colloid Interface Sci. 672 (2024) 715-723. https://doi.org/10.1016/j.jcis.2024.06.079.

37 Y. Zhu, Y. Liu, T. Ren, Z. Yuan, Self-supported cobalt phosphide mesoporous nanorod arrays: a flexible and bifunctional electrode for highly active electrocatalytic water reduction and oxidation, Adv. Funct. Mater. 25 (2015) 7337-7347. https://doi.org/10.1002/adfm.201503666.

38 Z. Fu, Z. Jiang, T. Hu, Z.-J. Jiang, Hierarchical nanoassembly of $Ni/MoS_2@Ni_{12}P_5/ZnP_2$ achieved by a plasma assisted phosphorization with highly improved electrocatalytic activity for overall water splitting, Electrochim. Acta 419 (2022) 140392. https://doi.org/10.1016/j.electacta.2022.140392.

39 D. Li, G. Hao, W. Guo, G. Liu, J. Li, Q. Zhao, Highly efficient Ni nanotube arrays and Ni nanotube arrays coupled with NiFe layered-double-hydroxide electrocatalysts for overall water splitting, J. Power Sources 448 (2020) 227434. https://doi.org/10.1016/j.jpowsour.2019.227434.

40 Y. Liu, Y. Bai, Y. Han, Z. Yu, S. Zhang, G. Wang, J. Wei, Q. Wu, K. Sun, Self-supported hierarchical FeCoNi-LTH/$NiCo_2O_4$/CC electrodes with enhanced

655 bifunctional performance for efficient overall water splitting, ACS Appl. Mater.
656 Interfaces 9 (2017) 36917-36926. https://doi.org/10.1021/acsami.7b12474.
657 41 F. Lv, J. Feng, K. Wang, Z. Dou, W. Zhang, J. Zhou, C. Yang, M. Luo, Y. Yang,
658 Y. Li, P. Gao, S. Guo, Iridium-tungsten alloy nanodendrites as pH-universal water-
659 splitting electrocatalysts, ACS Cent. Sci. 4 (2018) 1244-1252.
660 https://doi.org/10.1021/acscentsci.8b00426.
661 42 N. Jiang, B. You, M. Sheng, Y. Sun, Electrodeposited cobalt-phosphorous-derived
662 films as competent bifunctional catalysts for overall water splitting, Angew. Chem.
663 127 (2015) 6349-6352. https://doi.org/10.1002/ange.201501616.
664 43 P. Wei, X. Sun, Z. He, F. Cheng, J. Xu, Q. Li, Y. Ren, J. He, J. Han, Y. Huang,
665 Adenosine triphosphate induced transition-metal phosphide nanostructures
666 encapsulated with N, P-codoped carbon toward electrochemical water splitting, Fuel
667 339 (2023) 127303. https://doi.org/10.1016/j.fuel.2022.127303.
668